Marine and Petroleum Geology 91 (2018) 262–278

Contents lists available at ScienceDirect

Marine and Petroleum Geology

journal homepage: www.elsevier.com/locate/marpetgeo

Research paper

Evolution of porosity and pore geometry in the Permian Whitehill Formation of South Africa – A FE-SEM image analysis study

Kenneth Chukwuma[a,*], Emese M. Bordy[a], Angelique Coetzer[b]

[a] Department of Geological Sciences, University of Cape Town, 7701, South Africa
[b] Electron Microbeam Unit, Central Analytical Facilities, Stellenbosch University, 7599, South Africa

ARTICLE INFO

Keywords:
Whitehill Formation
Karoo shale gas
Amorphous organic matter
Organo-genetic pores
Thermal maturation
Thermochemical decarboxylation
Carbonate dissolution

ABSTRACT

Since the advent of technologically efficient exploitation of economic hydrocarbon reservoirs in shales, increasingly more research has been devoted to identifying and characterizing pore systems within shales. However, only a handful of these studies focused on the development of porosity in thermally mature unconventional reservoirs. In this study, the evolution of porosity and pore geometry in the Permian Whitehill Formation is addressed with the aid of ultrathin sections (2 × 3 cm, 10–20 μm thick) and field-emission scanning electron microscopy (FE-SEM) on samples with mean random vitrinite reflectance values ranging from 1.03 to 4.07 %Ro. We document a strong positive covariation of porosity and total organic carbon content (TOC) in all localities. However for samples with vitrinite reflectance values greater than 2.88 %Ro porosity per unit TOC decreased by over 25% relative to samples with lower thermal maturities. The positive covariation of thermal maturity and total porosity recorded here is unsurprising and have been documented previously in many gas shales. However, the dramatic decrease in porosity restricted to samples from localities that experienced advanced maturation (Ro > 2.88%) is viewed as an evidence that porosity decrease is directly related to late thermal decarboxylation of organic matter. This is supported by the presence of pores and micro-fractures infilled by fibrous grains, including carbonates, clays, silicates, and phosphates, and residual fluid inclusions. These grains were likely generated from re-precipitation of framework grains previously dissolved by organic acids (carboxylic, phenolic) that were generated during thermochemical decarboxylation of the OM. Our findings do not only fill important gaps in the understanding of organic pore development, including processes that create, preserve, and destroy porosity, the porosities described here are also key to gas transfer from shale matrix to induced fractures during fracture stimulation programs.

1. Introduction

Traditionally, it is believed that hydrocarbons (oil and gas) are generated within organic matter-rich shales (i.e., source rocks) and then migrate into more porous units (i.e., reservoir rocks), such as sandstone, conglomerates or limestone and other naturally fractured rocks types (e.g., Demaison and Huizinga, 1991; Klemme and Ulmisheck, 1991; Magoon and Dow, 1994). However, appreciable hydrocarbons formed in some source rocks are retained after their formation, especially where the source rocks are highly impermeable or “tight”, resulting in an unconventional situation where source rocks also serve as reservoirs for hydrocarbons (e.g., US-NPC, 2007; Boyer et al., 2011; Wright et al., 2015). A gas shale is a peculiar type of unconventional gas-hosting rock in which the gas content can only be extracted by fracture permeability, either via artificial hydraulic fracturing (fracking) or via natural fractures (e.g., Jarvie et al., 2007; US-EIA, 2011). The cost-effective exploitation of economic hydrocarbon reservoirs in shale successions has resulted in a significant increase in funding of investigations on pore structures in shales (e.g., Loucks et al., 2009; Bernard et al., 2013; Milliken et al., 2013). Whether a shale can be suitable for gas production or not depends on the content and nature of its organic matter, porosity and ductility/brittleness (Jarvie et al., 2007; Passey et al., 2010). Characterizing the porosity in shales has been a rather difficult task, largely because of the small pore sizes of these rocks, much smaller than those in conventional reservoirs (Schieber and Zimmerle, 1998; Loucks et al., 2012; Camp et al., 2013). In addition, shales are dramatically heterogeneous with multi-level (from macro-down to nanoscale) variations in their structures and compositions (e.g., Curtis et al., 2012; Lazar et al., 2015). This means that each shale play is unique in several geological aspects and cannot be used with ease to evaluate another play, not even those in the same shale unit.

In addition, from a scientific standpoint, porosity is a multifaceted

* Corresponding author.
E-mail address: chkken003@myuct.ac.za (K. Chukwuma).

https://doi.org/10.1016/j.marpetgeo.2017.12.026
Received 22 June 2017; Received in revised form 24 August 2017; Accepted 17 December 2017
Available online 11 January 2018
0264-8172/

subject and is approached differently among disciplines. For instance, petroleum engineers and reservoir scientists quantify porosity using petrophysical (bulk) methods, such as helium porosimetry (e.g., Cui et al., 2004; Ross and Bustin, 2007; Mastalerz et al., 2013; Bahadur et al., 2015). While bulk characterization techniques effectively provide quantitation of pore throat dimensions (e.g., Dewhurst et al., 1998), they do not measure total porosity, which is critical for estimating the capacity of the reservoir. On the other hand, shale petrographers approach porosity development in shale successions by providing both quantitative and visual qualitative analyses of porosity by direct petrographic examinations of pores through the application of scanning electron microscopy and its auxiliary technologies (e.g., Loucks et al., 2009; Keller et al., 2011; Klaver et al., 2012; Camp et al., 2013; Milliken et al., 2013; Löhr et al., 2015). Direct observation of pores has a unique advantage of distinguishing pores within organic particles from those within the inorganic matrix of the shale sample. Although recent studies (e.g., Löhr et al., 2015; Sommacal et al., 2016) have shown that pores within OM have greater affinity for hydrocarbon than those within mineral grains, distinguishing OM-hosted- from mineral-hosted pores also allows porosity evolution to be related to factors closely associated with depositional, diagenetic, and catalytic processes (e.g., Curtis et al., 2012; Bernard et al., 2013; Schieber, 2013).

Pore networks within most gas shales are largely dominated by nanometer-size pores (e.g., Ross and Bustin, 2007; Curtis et al., 2012; Loucks et al., 2012; Milliken et al., 2013). IUPAC (1994) subdivided materials with nanometer-sized pores into three categories: macropores (> 50 nm), mesopores (2–50 nm), and micropores (< 2 nm). Characterizing nanometer-sized pores is challenging because conventional transmitted and reflected optical microscopy cannot image meso- and micropores due to the low power of magnification of these standard methods. While FE-SEM and its auxiliary technologies have the suitable resolution (Loucks et al., 2009; Curtis et al., 2012; Camp et al., 2013), this method is however not suitable for rock chips because of their irregular surface topography (Loucks et al., 2009; Keller et al., 2011; Schieber, 2013). Mechanically polished thin sections often contain artefacts such as abrasion marks and grinding debris (Schieber, 2013; Kaufhold et al., 2016), which can influence the detection of delicate features in SEM images. Ion-milling techniques, including those that involve the use of either a focused ion beam (FIB) or a broad ion-beam (BIB) of Ar + or Ga + to remove a small amount of material to generate an ultra-smooth surface (Loucks et al., 2009; Keller et al., 2011; Camp et al., 2013; Schieber, 2013), has greatly enhanced the understanding of shale features with SEM. However, ion-milling is limited due to the small field of view (about 40 × 30 μm) that can be imaged by SEM at sufficiently small pixel size at a time (Curtis et al., 2012; Kaufhold et al., 2016).

To date, the link between porosity and thermal maturity is inferred from studies that used samples with low thermal maturity range and where thermal maturity had been achieved through burial diagenesis (e.g., Cui et al., 2004; Ross and Bustin, 2007; Keller et al., 2011; Chalmers et al., 2012; Curtis et al., 2012; Bernard et al., 2013). Studies are rare on the development of porosity with increasing thermal maturity using samples with a wider range of thermal maturity and where thermal maturities were achieved through tectonic burial and thermal devolatilization during igneous intrusion. Samples from the Permian Whitehill Formation (WHF) in the main Karoo Basin of South Africa have thermal maturities that range between ~1.0 and > 4.0% Ro (Rowsell and De Swart, 1976; Cole and McLachlan, 1991). Works by Oelofsen (1981), Visser (1992) and Chukwuma and Bordy (2016) have shown that the WHF consists of subunits with remarkably uniform primary lithologic and sedimentologic characters across the Karoo Basin. In particular, the omnipresence of pyrites in both euhedral and framboidal forms, that appear to have formed due to the activity of sulfate-reducing bacteria at or near the depositional interface, is a strong evidence that uniform reducing (anoxic) conditions were persistent at all localities across the basin during the deposition of the lower two subunits (F1 and F2). Also, the 'consistency in the thickness of the biozones' (Oelofsen, 1981, p. 24) in the upper WHF subunits (F3, F4, F5) indicates that the depositional conditions were seemingly the same over the entire basin floor. There is, therefore, no evidence that depositional conditions varied significantly across the basin during the deposition of any of the five subunits of the WHF. This inference is important because it gives weight to the assumption that initially, each subunit of the WHF was identical in overall properties and that significant differences observed in abundance and distribution of porosity, particularly within organic macerals, are directly related to post-depositional (diagenetic and thermal maturation) processes, which were majorly controlled by the relative distance of each locality from the presumed heat source, the Cape Fold Belt (CFB). Rowsell and De Swart (1976) and Cole and McLachlan (1991) observed that the degree of thermal maturity (measured with reflectance of vitrinite, [%Ro]) show a progressive decrease from the southwest (heat source) to the northeast. In the study by the latter authors, samples from localities within about latitude 29 °S and more southerly were within late dry gas window (%Ro > 2.3) whereas those within latitude 31.5 °S and more northerly were within oil to the wet gas window (%Ro < 2.3).

The overall objectives of this study were to investigate the evolution of porosity and pore geometry with increasing thermal maturity and to assess the relationship between TOC and total porosity in reservoir shales. In order to realize these goals, visual qualitative and quantitative image analyses of the pore systems within the WHF were combined with suites of geochemical analyses. We examined high-resolution two-dimensional (2-D) FE-SEM images of ultrathin sections (2 × 3 cm, 10–20 μm thick) from samples taken from three major subunits (F1-F3; Chukwuma and Bordy, 2016) of the WHF across the Karoo Basin (Fig. 1). X-ray fluorescence spectroscopy, Rock-Eval pyrolysis, and elemental and stable isotope analyses provided data on the compositional geochemistry of the shale samples. The geology of the Karoo Basin and the WHF has been explained in detail in the literature [e.g., by SACS (1980), Cole and Basson (1991), Visser (1992), Catuneanu et al. (2005), Tankard et al. (2012), Geel et al. (2015)], and are not repeated here.

2. Samples, methods and analytical limitations

2.1. Samples

Samples used in this study come from 14 localities along the semi-continuous exposure belt of the WHF in the main Karoo Basin (Fig. 1A), representing a complete stratigraphic development of the WHF (Fig. 1B), including organic matter (ranging between < 1 and 16.5%), different burial depths and temperatures (with calculated thermal maturities ranging between < 1 and 4.6 %Ro) and thickness (ranges between < 10 to about 70 m). The sampling localities, including the type unit of the WHF (Cole and Basson, 1991), were targeted because they expose the same stratigraphic subunits of the shales but at different distances from the CFB (Rowsell and De Swart, 1976; Cole and McLachlan, 1991). The largely unweathered samples were taken with a STIHL E-Z Core Rock Drill fitted with a Pomeroy 40 × 2.5 cm core barrel. The samples are designated by abbreviations related to their localities, e.g., PAT for Prince Albert, LAG for Laingsburg, MAJ for Matjiesfontein, CAL for Calvinia, NUW for Nuwelande, LOE for Loeriesfontein, VAK for Vanwyksvlei, BTT for Britstown, STY for Strydenburg, HPT for Hopetown and CST for Christiana. The description of the lithology and sedimentary structures of the samples is provided by Chukwuma and Bordy (2016).

2.2. Whole-rock and organic carbon composition

The chemical composition of One-hundred-and-twenty (120) powdered samples was determined using standard X-ray Fluorescence (XRF) procedure (Injuk and Van Grieken, 1993; IAEA, 1997) in the

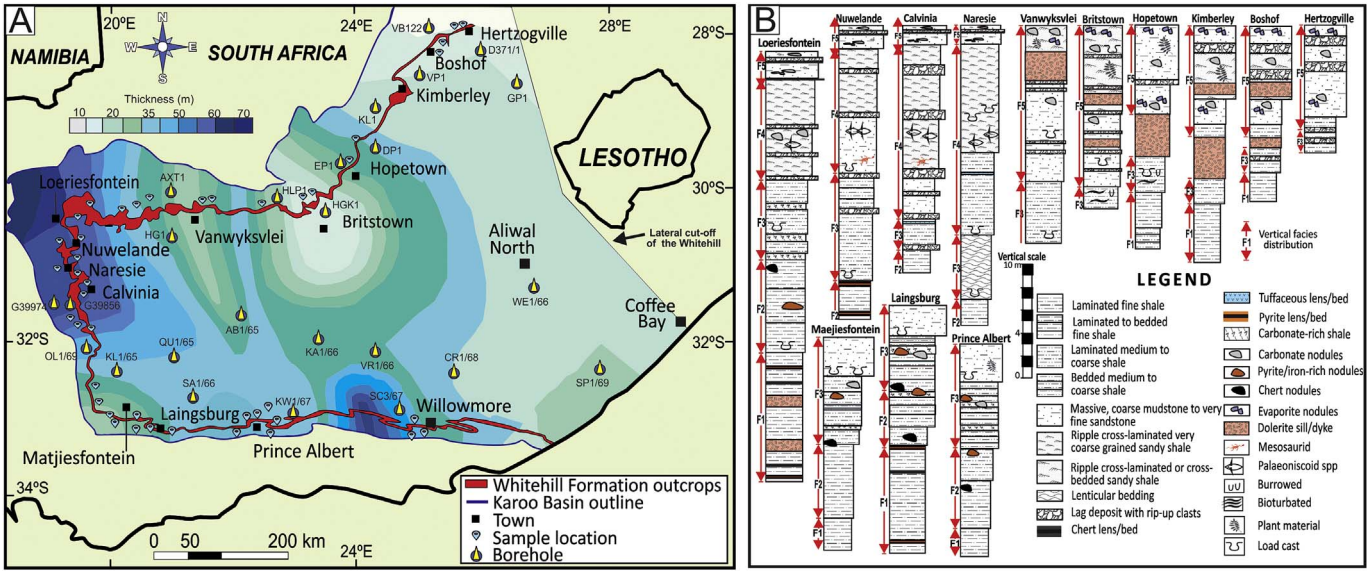

Fig. 1. A: Map of the southern main Karoo Basin and the semi-continuous outcrop belt of the Whitehill Formation (WHF). The thickness of the WHF is based on borehole data from Rowsell and De Swart (1976) and Cole and McLachlan (1991). The locations of some of the boreholes and sample collection points are shown. **B**: Simplified sedimentological logs of the WHF measured at selected outcrops. The thickness reported in this figure is not the maximum WHF thickness at those localities, but the maximum exposed section. The WHF lithostratigraphy at Strydenburg is similar to that in Hopetown.

Department of Geological Sciences at the University of Cape Town. Total carbon, nitrogen and sulfur as well as stable isotopic compositions of organic carbon and nitrogen (Könitzer et al., 2012) were analysed for 30 selected samples using Costech Elemental Analyzer (EA) with zero-blank autosampler coupled to a ThermoFinnigan Delta Plus XL isotope ratio mass spectrometer (IRMS) at the Stable Isotope Laboratory of Iowa State University. 30 mg of each sample was wrapped in tin capsules and placed into the zero-blank autosampler, and then combusted in the EA. One full run comprising 49 positions (1 blank, 12 standards, and 36 samples) was performed. Isotope results were corrected to the appropriate isotopic scale using international reference standards (acetanilide, caffeine, cellulose, IAEA-N2). Elemental concentrations were calculated using reference standards and the sample gas intensities. The stable isotopic compositions are reported in the conventional delta-notation with respect to the Vienna Peedee belemnite (VPDB) standard for carbon, whereas the $\delta^{15}N$ of each sample is expressed relative to atmospheric dinitrogen. Analytical reproducibility is about ± 0.1‰ for both $\delta^{13}C$ and $\delta^{15}N$.

Rock-Eval pyrolysis (Espitalié et al., 1985; Bhattacharya and Dutta, 2015) was performed on 68 samples using Vinci Technologies Rock-Eval 6 instruments. Two-centimeter cube (2 cm^3) of each sample was weighed. The samples were pulverized to 60–100 mesh size in a brass mortar and weighed to 60 g. The measured samples were then collected in crucibles initially pulverized in an inert atmosphere of nitrogen in the pyrolysis oven. The initial temperature of the pyrolysis oven was maintained at 300 °C for 5 min. The temperature was then raised to 600 °C at a rate of 25 °C/min. The oxidation phase was conducted with temperature conditions similar to the pyrolysis oven but was raised to a maximum of 850 °C. Carbon steel rings (1 g, nominal carbon content of 0.8%) were used as internal standard verified against the acceptable range using a certified reference material (CRM) provided by the laboratory at the Indian Institute of Technology, Bombay. Thermal maturity (in vitrinite reflectance unit [%Ro]) was derived from T_{max} (°C) using the method described by Jarvie et al. (2001, 2007): %Ro (calculated) = 0.0180 × T_{max} − 7.16. The calculated %Ro values were largely in agreement with those measured from the reflectance of vitrinite by previous authors (e.g., Rowsell and De Swart, 1976, p. 107; Table 2).

2.3. Light microscopy and FE-SEM

One-hundred-and-forty-eight (148) pieces of whole rock with diameters of less than 5 cm selected from the fourteen localities (Fig. 1A) provided the sample base for petrographic (light/electron optical techniques) characterization of the rock textural attributes, fabric, mineralogies, and porosity. The samples were prepared into uncovered polished thin sections by surface impregnation with a mixture of low viscosity epoxy-resin and hardener in order to minimize mechanical impact. Hardening was performed at a moderate temperature (< 60 °C) and for a few minutes to avoid altering the fine organic details within the samples. These thin sections were then analysed by transmitted and reflected polarized light on a conventional petrographic microscope. A subset of the samples was prepared into 2 × 3 cm uncovered ultrathin sections (UTS; 10–20 μm thick). In order to minimize mechanical impact, prior to sectioning, the samples were placed into plastic mounting cups and were then held firmly with hardener. Two sides of the samples, one oriented perpendicular and the other parallel to bedding-plane, were ground using successive finer abrasives and then air-polished with fine (0.05 μm) silicon powder. Although this method does not produce the same level of ultra-smooth surfaces and resolution of less than 5 nm available with focused ion-beam (FIB) milling, these unusually thin polished sections can be used to acquire images with crisp resolution of shale features up to 8 nm without the usual artefacts associated with conventional (mechanically polished) thin sections. Lightly carbon/diamond-coated UTS were examined using a Zeiss MERLIN FE-SEM at the Stellenbosch University Central Analytical Facilities operated with 1) secondary electron (SE) using an accelerating voltage of 5 kV, a sample current of 250 pA at a working distance of 3 mm; 2) back-scattered electron (BSE) using an accelerating voltage of 20 kV, a sample current of 11 nA at a working distance of 9.5 mm; and 3) cathodoluminescence (CL) detectors. Cryo-energy-dispersive X-ray spectrometry (cryo-EDS) provided identification and characterization of components.

The general distribution and abundance of mineral crystals and OM were examined using a swath of ten images captured at 100-20 μm horizontal field width, machine magnification of 3000–1500× and pixel size of 5–20 nm/pixel using BSED. Additional characterization and component identification were made using CL detector and X-ray mapping. The distribution of pores was assessed using images captured

Table 1
Bulk chemical data of the WHF. Tsfur = total sulfur. Samples from Facies 5 were not analysed for organic compositions (Table 2).

Oxide/element	Facies 1 (n = 24)				Facies 2 (n = 24)				Facies 3 (n = 24)				Facies 4 (n = 24)				Facies 5 (n = 24)			
	Min	Max	Mean	SD	Min	Max	Mean	SD	Min	Max	Mean	SD	Min	Max	Mean	SD	Min	Max	Mean	SD
SiO_2 (%)	46.34	64.50	56.37	7.00	56.40	73.53	63.85	5.03	63.32	75.89	69.01	3.97	66.58	76.20	70.77	3.15	69.79	80.26	73.46	4.65
TiO_2 (%)	0.51	0.77	0.62	0.09	0.57	0.81	0.67	0.10	0.58	0.81	0.72	0.07	0.54	0.77	0.67	0.07	0.26	0.82	0.61	0.24
$A_{l2}O_3$ (%)	12.35	15.72	14.20	1.23	12.85	17.05	15.02	1.40	10.39	16.96	14.40	1.87	11.27	17.93	14.67	2.09	10.77	17.12	14.58	2.73
Fe_2O_3 (%)	1.25	9.79	5.03	4.90	5.70	12.82	7.51	2.40	0.38	3.67	1.09	0.94	0.24	2.11	1.04	0.60	0.38	1.22	0.71	0.41
MgO (%)	0.77	2.48	1.31	0.64	0.59	1.20	0.96	0.24	0.62	2.40	1.07	0.50	0.40	1.27	0.87	0.27	0.47	1.35	0.95	0.36
CaO (%)	0.78	1.02	0.92	0.49	0.89	1.34	1.13	0.24	0.06	0.57	0.20	0.15	0.08	0.94	0.33	0.29	0.14	0.26	0.18	0.06
Na_2O (%)	1.99	2.22	1.86	0.38	0.88	2.37	2.01	0.58	0.38	2.56	1.81	0.77	1.13	2.49	1.95	1.14	0.59	1.96	1.50	0.62
K_2O (%)	3.69	3.82	3.87	0.16	2.64	4.47	3.43	0.56	2.40	4.02	3.28	0.49	1.08	3.64	3.05	0.77	2.55	4.42	3.41	0.77
P_2O_5 (%)	0.05	0.49	0.19	0.20	0.14	0.39	0.21	0.11	0.05	0.13	0.09	0.04	0.05	0.16	0.08	0.03	0.04	0.08	0.06	0.20
T_{sfur} (n = 30)	0.81	7.88	3.24	1.72	0.68	8.22	3.83	2.08	0.25	2.40	0.71	0.73	0.17	1.48	0.72	0.44				
TOC (%)	2.06	9.61	6.15	2.92	1.67	16.50	6.22	3.31	0.30	3.91	2.04	1.14	0.48	1.80	1.03	0.67	–	–	–	
CIA	65.66	69.01	68.11		67.58	74.45	69.57		70.34	78.53	73.13		71.72	83.11	73.35		72.85	86.63	76.07	
δ^{13}Corg (n = 30)	−20.22	−18.57	−19.50	0.65	−22.32	−15.57	−18.91	2.55	−21.52	−18.30	−20.15	1.15	−24.71	−20.94	−22.42	1.92	–	–	–	
δ^{15}N (n = 30)	9.52	11.88	10.92	0.79	7.55	12.49	10.49	1.78	4.30	6.88	5.24	1.13	3.04	6.15	4.93	1.62	–	–	–	
C/N	2.13	16.47	9.54	5.73	0.77	2.48	1.50	0.75	0.32	12.38	2.32	3.28	4.83	43.70	17.62	13.27	–	–	–	

at 20–2.0 μm horizontal field width at a magnification of 15,000–200,000× and pixel size between 20 and 2 nm/pixel. In order to avoid nonrepresentation, samples were uniformly selected to include the full range of TOC values and thermal maturities, however, preference was given to areas with higher pore concentration so that a sufficient number of pores can be imaged for comparison. A subset of the samples was solvent extracted using the method of Radke et al. (1986) in order to differentiate bitumen from kerogen, using a solvent mixture, which comprised 90% dichloromethane and 10% methanol in the Chemistry Department at the University of Cape Town for 68 h at room temperature. The samples were air-dried and subsequently prepared into UTS and FE-SEM imaged. For pore analysis, all samples were observed on surfaces perpendicular to bedding.

2.4. FE-SEM identification of shale constituents

The composition of samples including, mineralogy, OM, grain/crystal boundaries were distinguished using back-scattered electron (BSE) detector, which has the ability to record variations in composition using the mean atomic number. Materials with a low atomic number such as carbon exhibit low BSE intensity and is scaled as darker regions; whereas a material with a high mean atomic number exhibits high BSE intensity and is scaled as lighter regions. EDS mapping taken across images allowed quantitation and identification of various shale components, including matrix composition, grain/crystal boundaries (Fig. 2).

2.5. FE-SEM pore identification and classification

Secondary electrons (SE) are generated at shallow depths (few nanometers) within the samples and their strength is dependent on the number of electrons that escape from the surface to reach a detector. Areas emitting more SE appear bright. Edges and angles on surfaces have a shorter distance to the detector, hence SE is suitable for identifying slight topographic variations (pores and textural features) which appear brighter relative to the flat and uniform areas in a sample.

The pore classification scheme presented here (Fig. 3) is based on observations made in this study, and therefore it is ad-hoc and exclusive to this study, although it is hoped that the approach can be used, with relevant alterations, in other studies as well. Pores were classified according to the nature (organic/nonorganic) of particles they were associated with. Distinguishing organic from nonorganic pores was necessary in order to relate porosity, pore size distribution, and other shale characteristics to mechanical and geochemical processes. The three types of pores observed are (Fig. 3):

1. Organic pores: defined based on the presence of OM along at least three sides of the pores or for > 75% of the diameter of the pore (in the case of circular pores).
2. Nonorganic pores: are surrounded by > 75% of the nonorganic material.
3. Mixed organic/nonorganic pores: are surrounded by mixed organic and nonorganic materials. They occur where one or two sides of the pores or less than 75% (in the case of circular pores) abut OM or nonorganic grain.

Organic pores are divided into three subcategories based on their size and shape (Fig. 3; Walls and Sinclair, 2011):

1. Bubble pores: are rounded to irregular shaped and are predominantly associated with intergranular OM and grain contact areas. They can occur singly or within one clearly visible principal area with several subparts in the form of alveolar networks. They range in size from about 100 nm to a few microns in diameter (Fig. 3B)
2. Foam pores: are similar to bubble pores (though generally more

Table 2
Distribution of organic compositions, pore size and total porosity in the WHF. * Average values from Rowsell and De Swart (1976, p. 107). In order to ensure the reliability of Rock-Eval data, only samples with minimum TOC of 0.5 wt.% and S2 of ~0.2 mg HC/g rock are used in this study. Average sample data are reported.

Location		Facies Code	Sample Code	OM Type	TOC (wt.%)	Tmax (°C)	Calc. %Ro	Average %Ro*	S1 - (mg/g)	S2 - (mg/g)	S3 - (mg/g)	HI (S2/TOC)	OI (S3/TOC)	Pore type distribution			Porosity (Area%)			Porosity/TOC
Latitude (dms)	Longitude (dms)													No of pores/ 200 μm^2	% Organic pores	% Nonorg. pores	Macro	Meso	Total	
33 14 31	21 51 26	F1	PAT1A	II	5.90	607	3.77	4.28	0.49	0.24	0.81	4.07	13.73	1318.00	86.23	13.77	2.32	2.46	4.78	0.81
33 13 51	21 42 10	F2	PAT2A	II	3.53	586	3.64	4.28	1.26	0.88	1.17	24.93	33.14	983.00	72.60	27.40	1.46	1.37	2.83	0.80
33 14 20	20 51 58	F2	LAG2C	III	7.88	546	3.39	3.81	0.14	0.43	0.87	5.00	11.00	1807.00	84.22	15.78	3.74	2.66	6.40	0.81
33 11 06	20 48 33	F2	LAG3A	III	3.90	526	3.27	3.81	0.30	0.18	1.75	4.62	45.00	1163.00	60.75	39.25	2.01	1.40	3.41	0.87
33 11 06	20 48 33	F2	LAG1A	II	5.23	501	3.11	3.81	1.80	1.37	2.25	26.00	43.00	1433.00	89.03	10.97	2.66	1.81	4.47	0.85
33 14 20	20 51 58	F2	LAG2B	II	8.44	494	3.07	3.81	0.60	0.16	2.72	2.00	32.00	2564.00	87.51	12.49	4.13	3.05	7.18	0.85
33 14 20	20 51 58	F2	LAG2A	II	5.58	488	3.03	3.81	0.17	0.35	2.51	6.00	45.00	1624.00	77.59	22.41	2.55	2.31	4.86	0.87
33 08 22	20 21 08	F1	MAJ2B	II	6.36	488	3.03	3.35	2.82	26.33	0.35	413.99	5.50	2008.00	81.38	18.62	3.48	1.81	5.29	0.83
33 11 03	20 48 45	F2	LAG5A	III	2.93	484	3.01	3.81	0.50	0.15	1.03	4.00	35.00	695.00	68.22	31.78	1.45	1.03	2.48	0.85
31 06 01	19 29 06	F2	LOE4B	III	0.72	457	2.84	2.27	0.04	0.49	0.51	68.00	71.00	355.00	61.49	38.51	0.57	0.17	0.74	1.03
30 56 49	19 25 39	F1	LOE2B	II	6.03	454	2.82	2.27	0.61	5.12	0.56	84.91	9.29	2314.00	86.55	13.45	3.36	2.92	6.28	1.04
29 56 50	23 40 11	F1	STY 1A	II	2.06	448	2.78	1.60	4.72	7.18	0.39	348.54	18.93	1037.00	72.03	27.97	1.73	1.25	2.98	1.45
33 08 22	20 21 08	F1	MAJ2A	II	7.18	443	2.75	3.35	2.93	38.09	0.39	530.50	5.43	3048.00	91.21	8.79	4.60	3.05	7.65	1.07
31 14 25	19 42 49	F3	CAL3A	III	1.21	441	2.74	2.27	0.33	0.49	0.23	40.00	19.00	575.00	62.62	37.38	0.73	0.66	1.39	1.15
31 14 25	19 42 49	F3	CAL2B	III	1.35	439	2.73	2.27	0.14	0.33	0.26	24.00	19.00	786.00	63.87	36.13	1.03	0.51	1.54	1.14
30 56 49	19 25 39	F1	LOE2A	II	9.27	437	2.71	2.27	0.46	4.80	0.33	51.78	3.56	3682.00	93.65	6.35	6.04	3.77	9.81	1.06
30 56 49	19 25 39	F1	LOE1A	II	9.27	432	2.68	2.27	0.30	3.40	0.24	37.00	3.00	3317.00	94.44	5.56	5.78	4.15	9.93	1.07
30 56 49	19 25 39	F1	LOE1B	II	6.78	432	2.68	2.27	0.24	4.13	0.62	60.91	9.00	3583.00	91.63	8.37	3.80	3.21	7.01	1.03
33 08 22	20 21 08	F1	MAJ1A	II	2.58	433	2.69	3.35	7.83	6.14	0.58	238.00	22.00	1466.00	84.51	15.49	2.03	1.62	3.65	1.41
33 08 22	20 21 08	F1	MAJ1B	II	2.34	426	2.65	3.35	3.15	4.56	0.83	195.00	35.00	1787.00	87.96	12.04	1.97	1.44	3.41	1.46
31 06 01	19 29 06	F2	LOE4A	III	0.72	428	2.66	2.27	0.15	0.93	0.64	129.00	89.00	463.00	78.33	21.67	0.28	0.38	0.66	0.92
33 08 17	20 21 07	F2	MAJ5A	III	1.26	426	2.65	3.35	0.60	0.18	0.88	9.00	70.00	616.00	68.85	31.15	0.77	1.09	1.86	1.48
31 14 25	19 42 49	F2	NUW1V	II	2.62	428	2.66	2.27	1.13	3.53	0.47	134.73	17.94	621.00	70.23	29.77	1.27	1.59	2.86	1.09
31 14 25	19 42 46	F3	NUW4	II	2.17	422	2.62	2.27	0.13	0.49	0.61	18.00	47.00	937.00	64.80	35.20	1.26	1.41	2.67	1.23
31 14 25	19 42 49	F3	CAL2A	III	3.70	417	2.59	2.27	0.60	0.25	0.40	4.00	11.00	6724.00	79.30	20.70	1.69	2.62	4.31	1.16
30 56 49	19 25 39	F2	LOE6B	II	8.83	408	2.53	2.27	0.60	0.18	0.16	2.00	2.00	3502.00	94.80	5.20	4.83	5.69	10.52	1.19
30 56 49	19 25 39	F1	LOE2/H	II	9.61	402	2.50	2.27	6.52	6.43	0.65	67.00	7.00	4066.00	92.63	7.37	5.41	6.63	12.04	1.25
30 56 49	19 25 39	F2	LOE3B	II	8.92	395	2.45	2.27	0.10	0.58	0.22	7.00	2.00	3182.00	90.40	9.60	4.92	5.07	9.99	1.12
31 06 45	19 28 52	F2	NAR2B	II	0.93	394	2.45	2.27	0.10	1.02	0.82	110.00	88.00	215.00	48.35	51.65	0.50	0.32	0.82	0.88
30 56 49	19 25 39	F2	LOE3A	II	9.51	358	2.22	2.27	0.40	1.35	0.19	14.00	2.00	3008.00	90.07	9.93	5.01	4.65	9.66	1.02
30 56 49	19 25 39	F2	LOE-C2	II	16.51	349	2.17	2.27	0.87	0.29	2.28	2.00	14.00	3614.00	93.58	6.42	8.27	6.70	14.97	0.91
31 14 25	19 42 46	F3	NUW2B	III	1.67	349	2.17	2.27	0.10	0.48	0.68	29.00	41.00	623.00	51.57	48.43	0.75	0.51	1.26	0.75
30 56 49	19 25 39	F2	LOE5B	II	9.13	343	2.13	2.27	0.30	0.23	0.10	1.00	1.00	4208.00	92.60	7.40	4.62	5.88	10.50	1.15
30 56 49	19 25 39	F2	LOE6A	II	9.26	339	2.11	2.27	0.60	0.21	0.41	1.00	4.00	3641.00	91.18	8.82	5.03	4.42	9.45	1.02
29 56 50	23 40 11	F2	STY 2A	II	2.06	339	2.11	1.60	4.72	7.18	0.39	348.54	18.93	827.00	72.24	27.76	1.08	1.39	2.47	1.20
31 14 25	19 42 49	F2	NUW1H	III	0.67	335	2.08	2.27	0.10	0.45	0.31	67.00	46.00	48.00	Na	100.00	0.59	Na	0.59	0.88
30 34 14	23 28 28	F3	HPT1A	III	3.91	332	2.06	1.60	0.13	0.17	0.44	4.00	11.00	1564.00	73.80	26.20	2.87	2.02	4.89	1.25
31 14 25	19 42 46	F3	NUW2A	III	2.11	332	2.06	2.27	0.11	0.48	0.43	23.00	20.00	634.00	71.88	28.12	1.29	1.05	2.34	1.11
30 56 49	19 25 39	F2	LOE-C1	II	9.87	317	1.97	2.27	0.30	0.98	0.59	10.00	6.00	428.00	89.42	10.58	4.90	6.87	11.77	1.19
31 06 45	19 28 52	F3	NAR2A	III	1.46	307	1.91	2.27	0.40	0.36	1.75	12.00	120.00	263.00	38.55	61.45	0.65	0.22	0.87	0.60
28 06 19	25 28 49	F3	CST3B	III	1.72	305	1.89	1.11	0.50	0.16	0.33	55.00	114.00	732.00	60.70	39.30	0.72	0.55	1.27	0.74

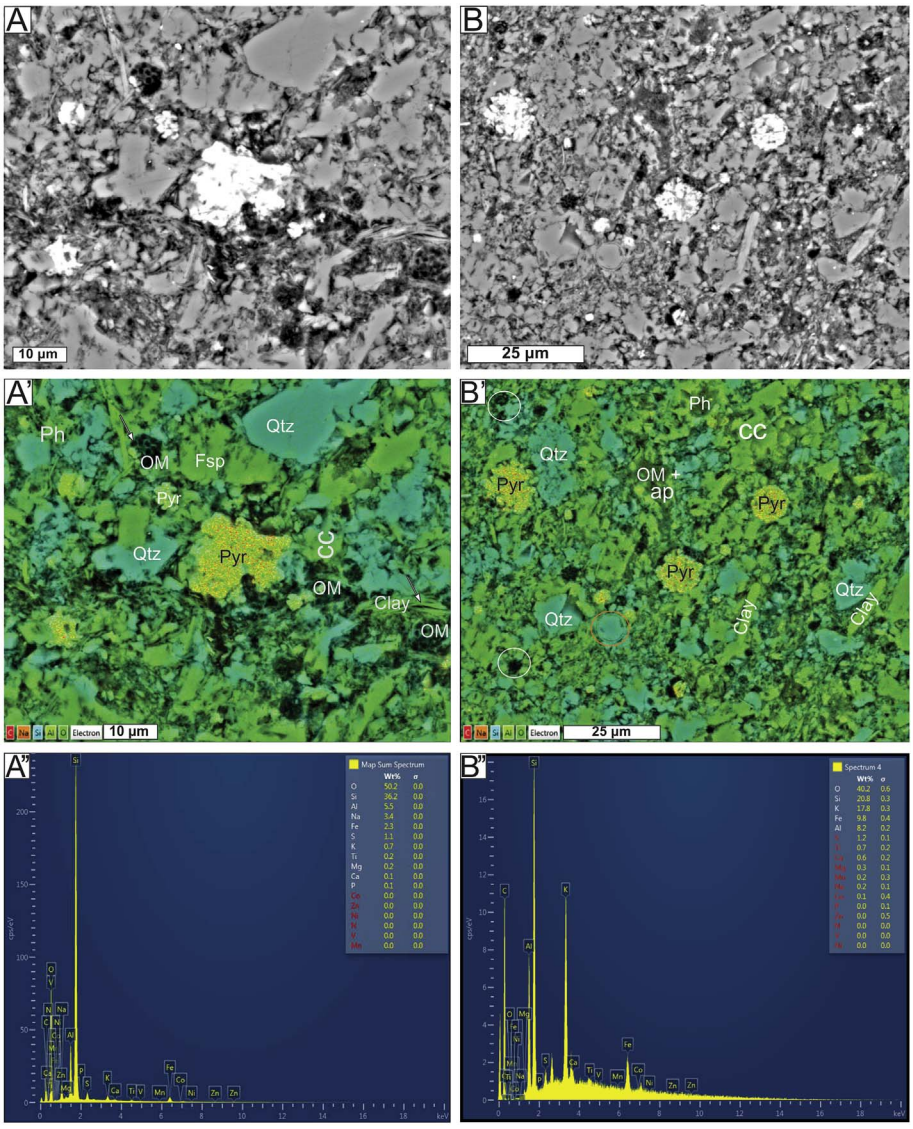

Fig. 2. A–B: Back-scattered scanning electron microscope images of shale matrix and its constituents used for EDS analysis. A′-B′: EDS maps showing the various constituents of a shale matrix. Organic matter (OM) appears dark, mineral grains takes various light colors and shades of grey (see color legend at the base of image). Quartz (qtz), phosphate peloids (ph), pyrite (pyr), carbonate (cc), feldspar (Fsp), apatite (ap). Some organic macerals are shown in white circle while silica filled Tasmanites cyst is in yellow circle. A″-B″: EDS line spectra and sum of the various mineralogic constituents. (For interpretation of the references to color in this figure legend, the reader is referred to the Web version of this article.)

abundant) and tend to occur mostly in clusters and range in size from a few to about 100 nm (Fig. 3B).

3. Microchannels and fractures (Fig. 3C): narrow cracks characterized by irregular fracture faces and occur mostly along bedding-planes (horizontal), although a few inclined to vertical fractures, mostly inter-connected to the horizontally-oriented ones, were also documented.

Nonorganic pores occur in two notable forms: 1) phyllosilicate pores (usually occurs in association with micas and clays representing spaces where cleavage planes have been separated by bending of a grain, as well as intergrain spaces held open where grains (micas/clays) failed to compact into parallel arrangement; Fig. 3D); and 2) dissolution pores refer to vuggy pores with no preferred orientation within and around framework grains (mainly carbonate but also in quartz, clays and organo-minerallic aggregates and may have resulted from carbonate dissolution and reprecipitation. They are most common in carbonate-rich intervals.

Note that a few of the pores detected in the samples may not be an intrinsic part of the shales. Sample retrieval (e.g., during coring), preparation (thin sectioning) and exposure to vacuum during imaging can result in desiccation features, including the formation of pores (e.g., Fishman et al., 2012; Milliken et al., 2013). However, the pores (artefacts) induced by these processes have characteristic elongate, crack-like morphology and commonly occur at the interface between organic and inorganic domains (Fig. 4D). Pores surrounding some grains (e.g., carbonate; circumcrystalline pores) can also result from post-coring desiccation. This is usually caused by acids generated from sulfur oxidation, as shown by the presence of calcium sulfate precipitate on the surface of some cores. We use these criteria to distinguish induced pores from naturally occurring pores. As a result, manual pore interpretation was applied in preference to automated pore recognition because the image grey levels with the natural pores significantly overlapped grey levels displayed with the induced pores.

2.6. FE-SEM pore analyses

Outline of pores was hand-digitized using CorelDraw® and subsequently colored in with a designated color for each pore type (Fig. 3). A total of 618 images displaying a total of 84 608 pores were then processed using ImageJ®, a public domain image-processing and analysis software available from United States Institute of Health (http://rebweb.nih.gov/ij/index.html). The distribution of the different pore sizes and types are as summarized in Table 2.

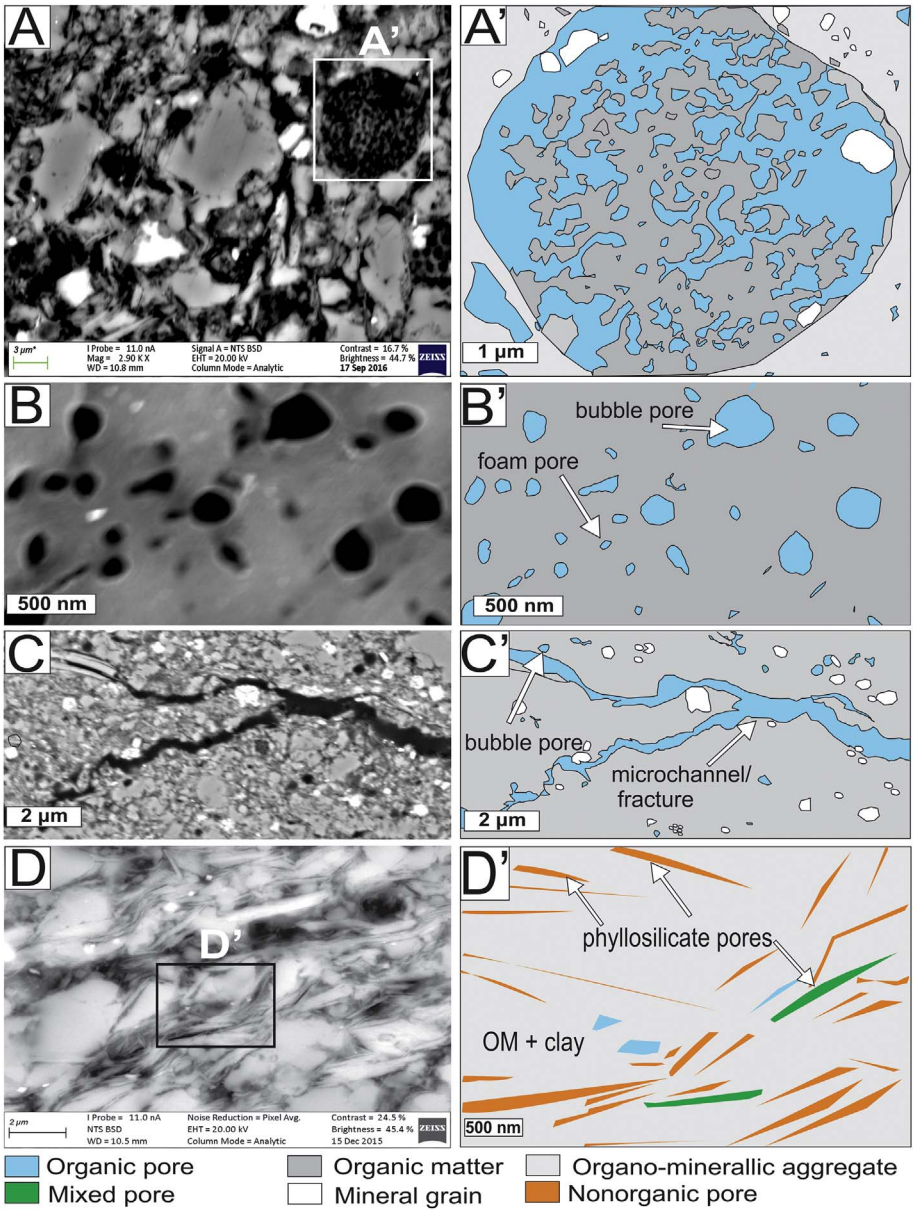

Fig. 3. Scanning electron microscope images (A–D) and their interpreted line drawings (A′-D′) illustrating the pore categorization scheme applied in this study. See section 2.5 for detail.

3. Results

3.1. FE-SEM and EDS observations

3.1.1. Nature and occurrence of mineral grains

The results from the bulk composition of the shales (Table 1) show that despite a sharp decrease in thermal maturation with increasing distance from the CFB, mineralogic compositions of the shales (Fig. 2) from the same stratigraphic subunit of the WHF are similar across the basin. Energy-dispersive X-ray measurements taken across several samples indicate that the shales are principally composed of silicates (predominantly quartz), clays, carbonates, iron sulfides (predominantly pyrite) as well as lesser volumes of phosphates and metal oxides (Ti, Ba). Quartz (in the form of single grains) is the chief component but significant amounts of chalcedony (radial fibrous with colloform textures), microquartz (crystal size smaller and/or up to 20 μm) and megaquartz (intergrown crystals with size > 20 μm; Schieber, 1996) were also present. Silicates occurred in two major forms: (1) as partial to complete replacement of certain microfossils (e.g., Tasmanites cysts and colonial algae cells; Fig. 5E–F) and other similar pores; and (2) as disseminated individual euhedral grains (Fig. 2). Overall, there are very few feldspars. Smectite, illite, mixed-layer clay, and chlorite are the chief phyllosilicate components while mica and biotite are minor. Mixed-layer clays and illite are more abundant in the southern part of the basin; whereas smectite and mixed-layer clay predominate the clay assemblages in the less-mature northern areas. The distribution of micas is uneven. Iron sulfides (chiefly as pyrite, lesser marcasite) occurred in various forms and predominantly in the lower two subunits (F1, F2). The two most common forms are: (1) partial to complete replacement of certain microfossils (colonial algae, few Tasmanites cysts, and similar pores); and (2) disseminated individual euhedral grains and framboidal/polyframboidal (bacterial) aggregates (Fig. 7C). Carbonates (dolomite and calcite) occur largely as disseminated individual euhedral grains. Carbonates peloids (pellets) are present in the lower intervals (F1 and F2) in most localities. Micrite becomes more abundant with increasing distance to the CFB, although some intervals (upper F2) are more enriched throughout the basin. Gypsum, which usually occurs in association with carbonates (as it is produced by the action of sulfuric acid [generated from oxidation of sulfur-rich OM] with carbonates; Geel et al., 2015), and phosphorites (Fig. 8C) are also

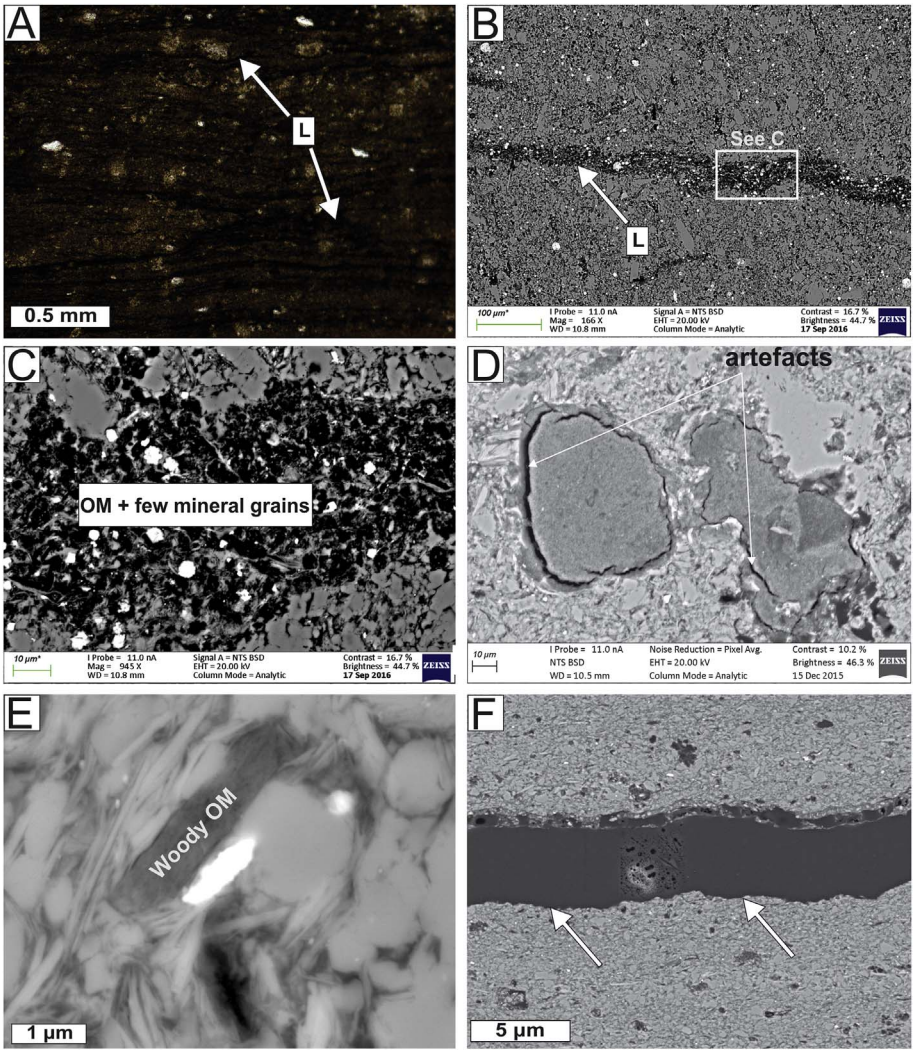

Fig. 4. Low magnification images illustrating the nature, abundance and distribution of organic matter (OM). A: Photomicrograph of shale matrix and associated OM concentrated into discrete elongate laminae and stringers (lamalginites). B: BSE image of abundant amorphous OM disseminated through the shale matric and intimately associated and aggregated with mineral grains. Rarer discrete OM laminae/stingers (L; arrowed) is also present. C: Close-up view of the OM laminae in B which consist of closely adjoined colonial algae. Both the amorphous and discrete OM domains in B are notably porous. D: Pores surrounding organic particles that likely resulted from desiccation during sample preparation and are not intrinsic part of the shale. E: Organic particle with distinctive curved, sharp edged appearance interpreted to be of higher plant (lignin/cellulose) origin. F: Fracture within shale matrix likely developed due to pore pressure increase prior to significant hydrocarbon generation and subsequently infilled with generated hydrocarbons.

documented and locally abundant in some intervals (e.g., upper F2 in Laingsburg). EDS analyses indicate that the latter is made up of phosphorus, calcium, oxygen, and fluorine, indicating that the mineral is likely apatite (ap). This apatite has a botryoidal texture, suggesting its origin was associated with microbial processes.

3.1.2. Nature and occurrence of organic matter

Two forms of organic matter (OM) are observed:

1. Structured organic matter (SOM) is identified mainly based on the retained morphological features of the ancient organisms to which the organic matter may be linked to and to a lesser extent on differences in relief and texture between the organic matter and the other shale constituents. Two structured organic macerals can be identified: Tasmanites cysts and colonial algae cells. The former can be identified based on its spherical to oval shape, thick cell walls, and relief/textural features of their infilled materials. The materials that infilled the walls of the Tasmanites cysts are usually different from those that fill their internal membrane (Fig. 5E–F). The cyst wall is composed of a lipoid-like substance (algenan) which is very resistant to chemical alteration and bacterial degradation (e.g., Tappan, 1980; Schieber et al., 2000). Infilling of the cysts usually starts from the inner wall and grew inward, retaining the original lipoid-like material of the walls. In scanning electron and optical microscopy, the appearance of this material is distinct and sharply contrasts with those of the cyst interior and can be used to identify cysts (Fig. 5E–F; Schieber et al., 2000). Colonial algae can be identified based on their spherical to oval shape, thin cell wall, and their occurrence in clusters (Figs. 4C, 5A–C and 7B). These organic particles lack the sharply defined arcuate edges that are consistent with fragments of cellulosic (woody) material, which further supports their interpretation as marine (Milliken et al., 2013).
2. Amorphous (unstructured) organic particles (AOM; Figs. 3A and 5A): The greater proportion of OM in the samples occur as homogeneous particulate debris that uniformly fills intergranular spaces and without any discrete form and can be described amorphinite (e.g., Teerman et al., 1995).

Both the structured and amorphous organic particles are disseminated throughout the shale matrix and closely aggregated with mineral grains in the form of organo-minerallic aggregates (Fig. 3A). They also occur in discrete laminae and organic-dominated domains with small mineral grains. Elongate, wavy and continuous laminae (lamalginite) composed of clusters of colonial algal cells (Fig. 4A–C), interpreted as algal mats by previous authors (e.g., Cole and McLachlan, 1991; Faure and Cole, 1999), are also common.

3.2. Organic matter, porosity and pores size distributions in selected sections

3.2.1. General statement

Results from the organic geochemistry, including thermal maturity and TOC, are listed in Table 2. TOC ranges between 0.72 and 16.5 wt.%

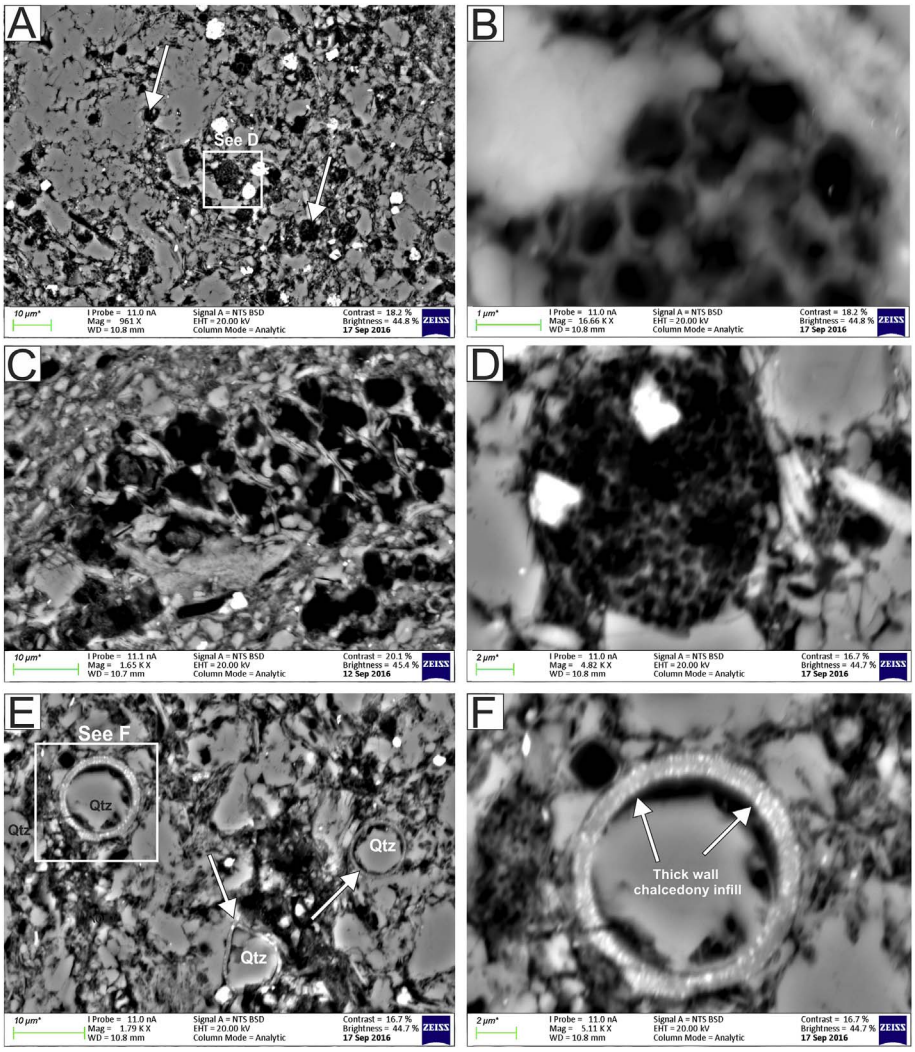

Fig. 5. A: Amorphous OM is typically present as organo-mineral aggregates and is porous, comprising a heterogeneous and complex network of pores in diverse sizes and shapes embedded with organic particles as well as mineral matter. B–D: OM of colonial algae origin usually contain homogeneous intercellular and intracellular pores due to partial collapse of the individual cells comprising the colony after compaction. Pores occur in three main size ranges: < 100 nm (most abundant, B, D), 100–500 nm (B, D) and 1–3 μm (C). E–F: OM identified as Tasmanites cysts based on its thick cell wall (arrowed) and oval shape (e.g., Tappan, 1980; Telnova, 2012) contains intracellular pores, representing partial silica infilling of the internal membrane.

(average of 5.15 ± 3.84 wt.% calculated from 48 samples). The pyrolysis S1, S2, and S3 were variable and range between < 1.0–7.83 mg HC/g rock, 1.0–38.09 mg HC/g rock, and > 1.0–3.0 mg CO2/g rock, respectively. Hydrogen-index (HI) and Oxygen-index (OI) ranged between 1.0–530.5 mg HC/g TOC and 1.0–425 mg CO2/g TOC, respectively. Pyrolysis Tmax ranges between < 410 °C and 607 °C, while thermal maturities range from 1.1 to 4.28 %Ro. OM (Table 2) is interpreted to be of marine or terrigenous origin based on Rock-Eval data and optical and electron microscope observations (Milliken et al., 2013), as well as stable isotopic composition of carbon and nitrogen (Meyers, 1997). The nature and distribution of organic matter, porosity and pore size and geometry in the WHF are illustrated with samples from the following seven representative localities.

3.2.2. Prince Albert samples

Based on SEM images (e.g., Fig. 6), the samples taken at the Prince Albert locality contain up to 30 area% of OM, whereas TOC values indicate an average of 4.42 wt.%. The high OM:TOC ratio is attributable to OM oxidation (removal of organic hydrogen and addition of oxygen to OM; Jarvie et al., 2007) in this locality, which has experienced the highest recorded thermal maturation (up to 4.07 %Ro; average of 4.28 from the study of Rowsell and De Swart, 1976). The OM is dominated by amorphous OM disseminated throughout the shale matrix and closely associated with mineral grains (Table 2). A few OM is concentrated in discrete OM domains (laminae; interpreted as lamalginites based on their elongated shape in both light and electron microscopes; Löhr et al., 2015) and recognizable organic detritus (Tasmanites cysts and colonial algal cells). The observed Tasmanites cysts appear as collapsed, flattened sutured discs, but a few are preserved in pristine condition and are preferentially infilled with silica and, therefore, are nonporous (apart from sheltered pores). The colonial algae cells are also largely collapsed, although a few are preserved in their original form, but are largely unfilled and porous. The organo-minerallic matrix is notably porous, comprising a complex network of equant, circular to angular pores in various size ranges but three size ranges are dominant: pores with a diameter of up to 50 nm, those with diameters ranging between 100 and 500 nm and those with diameter up to 3 μm (Fig. 5). The pores within the lamalginites and structured OM have similar morphology and narrower size range (Fig. 5B and D). They occur as equant circular pores with two size ranges: pores with diameter > 50 and those between 50 and 125 nm, although a few pores with diameter/long dimensions more than 1 μm are also present (Fig. 5C). Horizontal to subhorizontal microfractures are also abundant. A few of these organic pores are empty, while the majority are partially filled with kerogen, pyrite, carbonate, quartz, OM, and fibrous apatite (Figs. 4F and 6). The lamalginite contains abundant pores located between adjacent cells of colonial algae and within the cell membrane of the individual cells (Fig. 4C), indicating partial compaction and collapse of the individual cells that form the colony. However, in some organic-rich intervals where the thickness of the lamalginite and organic domains exceeds about 20 μm, the midsection of these organic macerals has been pervasively compacted leaving very little pore between and within the

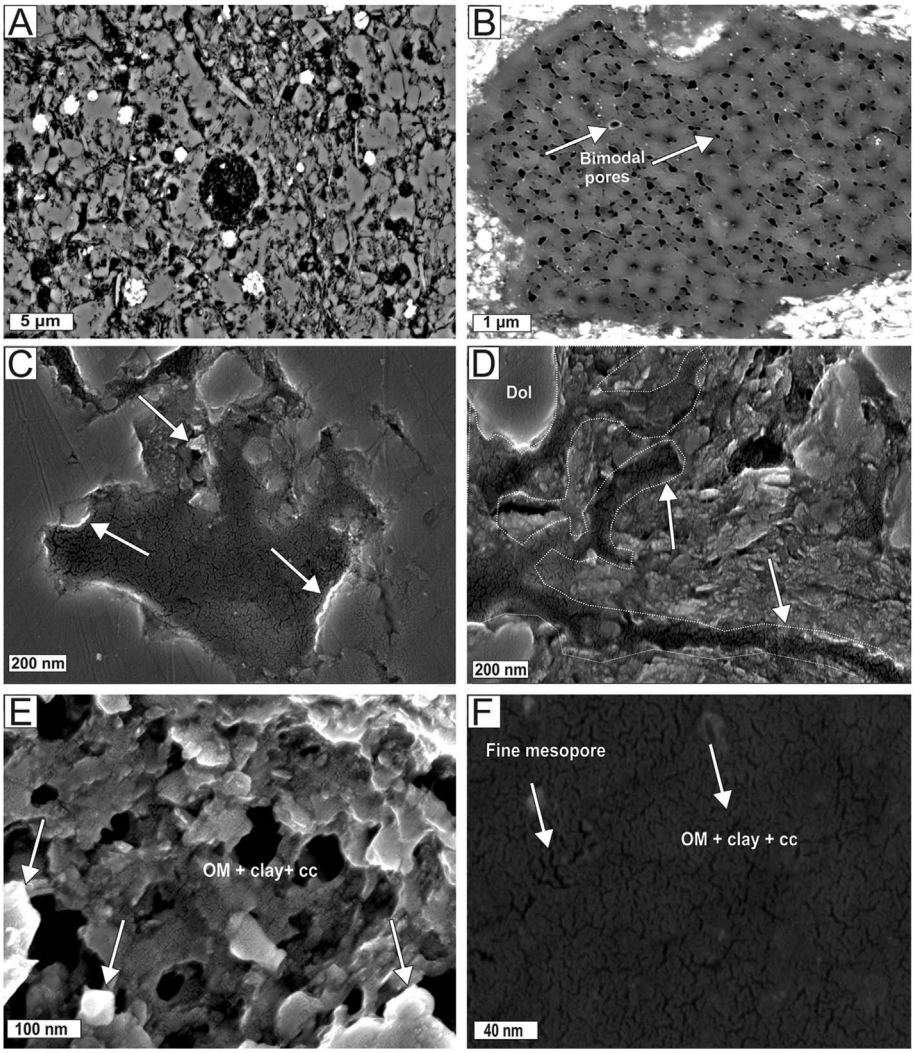

Fig. 6. A: Abundant heterogeneous pores in amorphous OM disseminated through the sediment. B: Residual OM (kerogen) containing pores (bubble and foam) typically left behind after exsolution of bitumen. C–D: Complex network of fractures infilled with residual fluid inclusion and diagenetic cements (mainly calcite and apatite) that likely reprecipitated during thermochemical decarboxylation of OM. E–F: Close-up view of secondary (diagenetic) cements (calcite, apatite, quartz) infilling pores and residual fluid inclusions. The cements occur on the borders of the fractures while the residual fluid inclusions are trapped in the central portions.

algal cells. Dissolution of carbonate and other framework grains created irregular/vuggy mesopores around these grains (Fig. 6C–F). These pores are not preferentially oriented horizontal to sub-horizontal, parallel to laminae but are somewhat interconnected (dotted outline in Fig. 6D). Carbonate and phosphatic filled microchannels (veins) are abundant in samples taken east of Prince Albert (Fig. 6E–F). Solvent extraction has little effect on the structures and pores within the lamalginites and some discrete organic domains but increased the abundance of the mesopores within amorphous OM in the shale matrix.

In the upper subunits of the WHF, the shale matrix is not dominated by pervasive organo-minerallic aggregation, rather OM occurs in patches of various sizes surrounded by the inorganic grains. No Tasmanites cysts were recorded and the number of colonial algae has reduced considerably. Several horizontal microchannels and microfractures (Mf), mostly filled with fibrous crystals (carbonate, silica, phosphate) are observed. Few sponge-like, porous residual pyrobitumen are also recorded (Fig. 6B).

3.2.3. Laingsburg samples

OM represented about 15–20 area% of the samples based on SEM images, which is consistent with TOC of up to 9 wt.% (average of 4.88 wt.%). The lower subunits of the WHF in Laingsburg, similar to samples from Prince Albert, are dominated by AOM and SOM disseminated through the shale matrix and closely associated with mineral matter and in lamalginites, however, the samples here contain more colonial algae cells, and fewer Tasmanites cysts (Fig. 7). The organic pores observed in the AOM are similar to those in Prince Albert samples, however, they contain more foam pores and fewer bubble pores. In the lower subunits, the majority of the pores contain kerogen residue and are filled with quartz, carbonate, and apatite similar to those in Fig. 6C–F. Microcracks infilled with OM, carbonates and quartz are abundant as well as sub-horizontal fractures (bedding plane parting) are seen cutting through the kerogen-mineral aggregates. From several FE-SEM images, samples have a porosity of up to 7.72 area%. Organic pores in the upper subunit (F3) have a wider size distribution, ranging from 400 nm to 3 µm, and are irregular in shape. Nonorganic pores are developed with clay mineral aggregates and range in size between 20 and 80 nm. A total porosity of about 4.8 area% is recorded. Pores within the silt-rich upper subunits of the WHF occur within carbonate grains and show evidence of dissolution and reprecipitation. Solvent extraction shows the similar effect to that recorded for the Prince Albert samples.

3.2.4. Matjiesfontein samples

OM represented about 15–20% of the sample area. The samples here are less dense, weighing only 1.14 g/cm^3. Colonial algae occur in long wavy lamalginites and discrete patches within the matrix. Tasmanites cysts are few and partially filled with microquartz while colonial algal cells are more in number and are partially filled with pyrite and quartz. Both are seen disseminated within the matrix. In the upper subunits of the WHF, OM occurs in discontinuous laminae and irregular patches. Elongate microfractures occur beneath the OM domains. Pores within

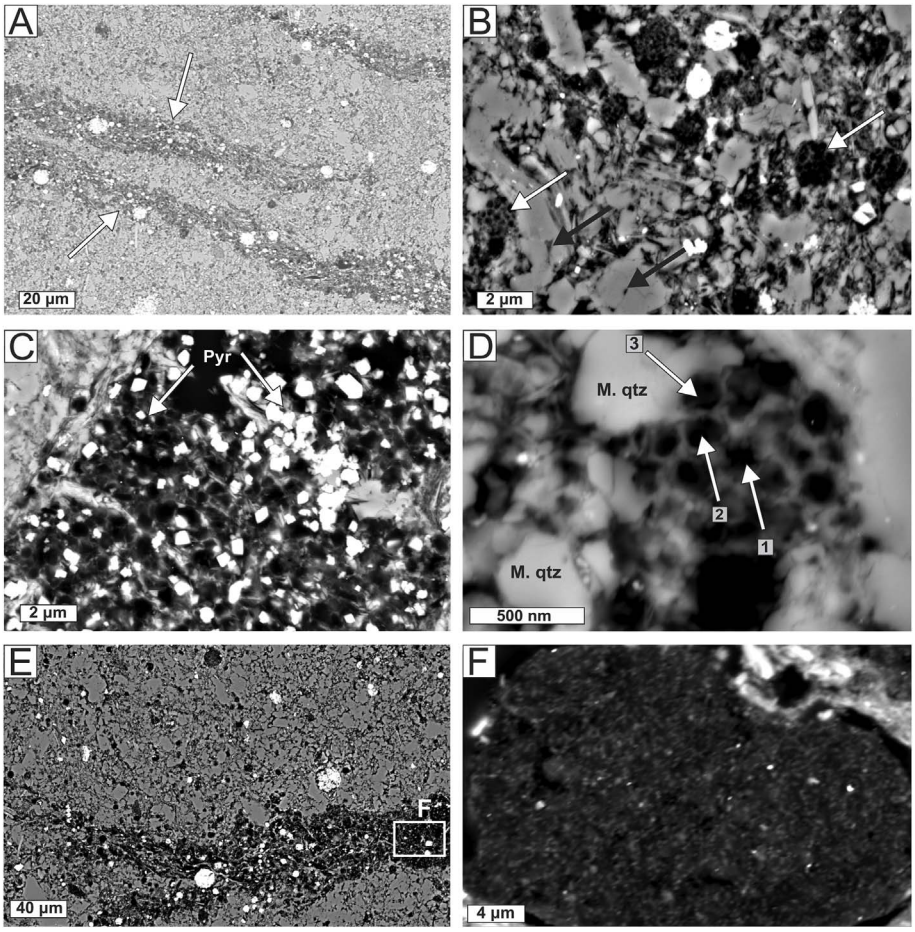

Fig. 7. SEM micrographs of the WHF samples in Loeriesfontein locality. A: Shale matrix dominated by OM concentrated in discrete domains that forms elongate porous laminae and stringers. B: OM intimately associated with mineral matrix comprising both pores with organic macerals (white arrow) and inorganic grains (black arrow). These pores are not homogeneously distributed through the shale matrix. C: Abundant and homogeneously distributed pores within OM domains, partially infilled by diagenetic pyrite (arrowed). D: Close-up view of the complex network of pores with amorphous OM. Pores within structure OM show homogeneous distribution and in 80–125 nm size range (arrowed). E–F: Concentration of OM into larger laminae and stringer with little mineral grains results in greater compaction and concomitant reduction of porosity in higher TOC samples.

the membrane of algal cells are homogeneous in shape (equant, circular) and size (range between 40 and 130 nm), whereas pores within organo-minerallic aggregates occur in various shapes and sizes. Elongate microfractures (bedding-plane partings) occasionally interconnect with pores within the matrix. Nonorganic pores are dominated by pores that may have been developed by carbonate dissolution and subsequent fluid inclusion processes during deeper burial. Triangular phyllosilicate platelet pores containing kerogen residue are also noted.

3.2.5. Calvinia and Nuwelande samples

OM represented 5–10% and 10–15 area% of Calvinia and Nuwelande sample area, based on FE-SEM images, and is consistent with reported average TOC values of about 2% and 4%, respectively. Calvinia samples are not characterized by abundant organo-minerallic aggregates, rather OM occurs in a few discrete patches. Organic particles in samples taken closer to dolerite sills are largely nonporous (i.e., SEM visible pores) and dense (1.38 g/cm^3), appear baked, and with high thermal maturity (%Ro > 3.8). These are interpreted as pyrobitumen and not kerogen macerals. Nuwelande samples contain a few large porous organic domains, which are likely preserved in compaction sheltered areas provided by the presence of cement. The pores within the organic domain are heterogeneous with some associated with euhedral pyrite grains. Pores within phyllosilicates are also observed and are similar to those in Fig. 8. Elongate microfractures (bedding-plane partings) were also observed and are thinner than those in Prince Albert.

3.2.6. Loeriesfontein and Strydenburg samples

OM represented about 20–30 area% of the samples based on SEM images, which is consistent with TOC of up to 16.5 wt.% (average of 8.3 wt.%). In the lower subunits, OM occurs in disseminations and in larger (up to 25–50 µm thick) and elongate lamalginites (Fig. 7A). The mid-section of the larger organic domains observed here contains little mineral grains and cement and were compacted resulting in a dramatic reduction in pore size and abundance (Fig. 7F). Recognizable organic detritus includes silt-sized Tasmanites cysts, colonial algal cells and macerals with smooth-texture and defined outline (interpreted to be of a higher plant origin; Fig. 4E). The organo-minerallic matrix is notably porous, comprising a complex network of pores, which ranges between > 50 and 1 µm. Another set of pores with diameters of up to 3 µm were also observed. The distinct organic domains are marked by pores that occur in defined shapes and sizes: equant, circular-sub angular, and < 25–500 nm and > 50–118. The pores are empty, but a few are partly filled with pyrite, carbonate (micrite) and quartz grains. Nonorganic pores are well-developed particularly within clay mineral aggregates and range in size between 20 nm and 3 µm (Fig. 8A–B, D–F).

4. Discussion

4.1. General trends

In general, the samples of the WHF represent a pore system that is strongly influenced by organic porosity. A strong positive covariation of TOC (wt.%) and total porosity (area%; measured with ImageJ using manually digitized FE-SEM images) exists in all localities (Fig. 9). Although not all pores are readily evident using electron imaging techniques, the trend line for TOC versus porosity intersected a TOC of zero at a positive porosity of about 1.4 area%, indicating that nonorganic porosity contributed about 1.4 area% of the total porosity documented. The positive covariation between OM and total porosity recorded here is unsurprising and predictable, given that these pores were presumably generated during thermal decomposition of OM and has been noted

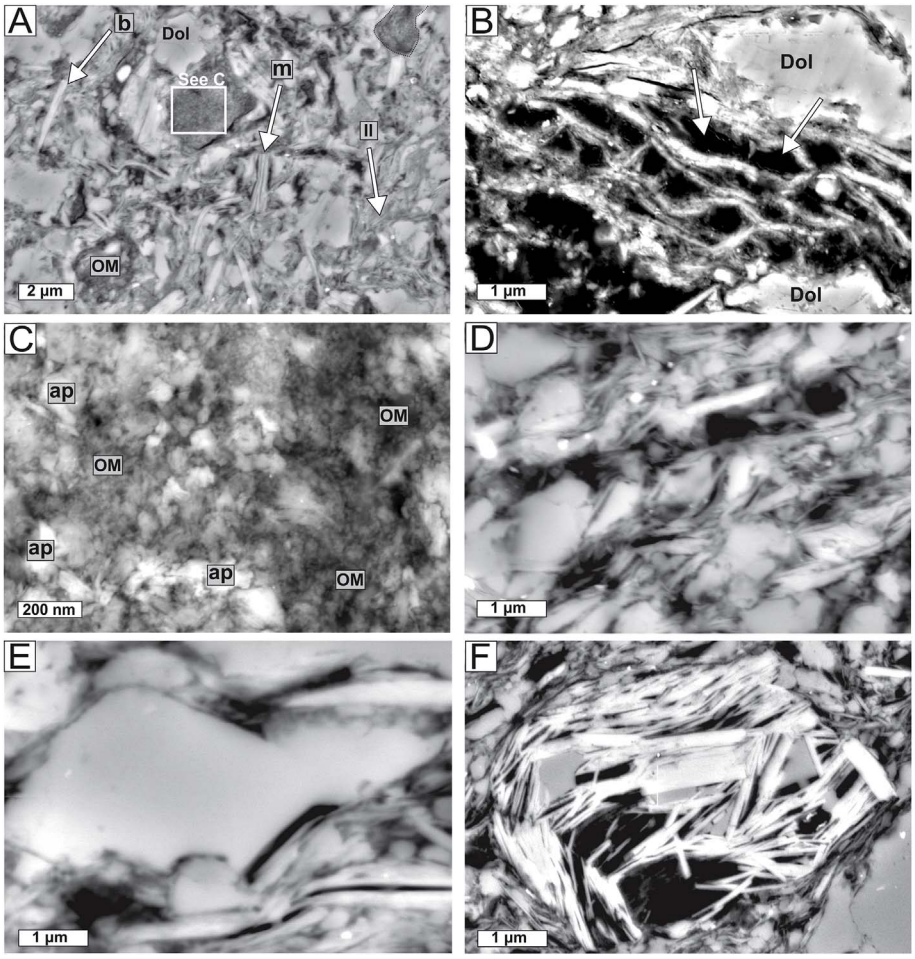

Fig. 8. SEM micrographs of the WHF samples in Strydenburg and Hopetown localities. A: Microlaminated shale matrix dominated characterized by subvertical-orientated elongate grains, amorphous OM closely associated with abundant clay minerals and binary OM and apatite composites. B: Phyllosilicate network pore created from exfoliation of elongated and subparallel oriented mica books; dol = dolomite. C: Close-up view of binary OM and apatite mixture. D–F: Porous OM-clay aggregates.

previously in several gas shales (e.g., Passey et al., 2010; Chalmers et al., 2012; Loucks et al., 2012; Bernard et al., 2013; Milliken et al., 2013). However, it was observed here that the positive covariation between TOC and total porosity is stronger for values of TOC between 2.03 and 5.4 wt.%. From Fig. 9, at lower or higher TOC values, a weak and nonsystematic covariation was detected between TOC and porosity. At TOC of < 2.03 wt.%, porosity either rises to as high as 1.8 area% or drops as low as less than 0.3 area%. Also, at TOC of > 5.4 wt.%, porosity increased in an irregular fashion relative to TOC. In the organic matter-hosted pore system of the Marcellus Formation, Milliken et al. (2013) observed that shale samples with a TOC of less than 5.5 wt.% had a positive correlation with porosity, whereas samples with TOC greater than 5.5 wt.% displayed little or no increase in porosity with more increase in TOC. Comparison of their results with this study shows some important similarities as well as marked differences. Most notable is the indirect proportional relationship between OM contents and porosity at TOC contents above 5.5 wt.%. However, in their study, a positive correlation exists in all values of TOC less than 5.5 wt%, whereas our results indicate that there was no such correlation for samples with TOC contents < 2.03 wt.%. Also, while these authors recorded a general decline in porosity for TOC values above 5.5 wt.%, our results show that in some locations, samples with TOC values > 5.5 wt.% show a relative increase in porosity. These differences could be related to a number of factors, including levels of thermal maturation, nature and type of organic matter, mineral assemblages and burial/diagenetic pathways as well as the quality of SEM images and the sampling bias that may have been introduced by imaging more porous intervals. It is noteworthy to state here that the decrease in total porosity in some of the higher TOC samples with thick and elongate stringers of OM domains with little or no mineral grains and cement may be related to the greater compaction of these OM domains, which resulted in drastic reduction in pore size and abundance (Fig. 7E–F).

4.2. Organic matter type

Small-scale variations in pore abundance, character and distribution were documented between the two distinct assemblages of OM throughout the localities sampled. Whereas the great majority of the OM occurs in the form of AOM, the majority of the pores are concentrated within discrete OM domains and stringers, comprising mostly colonial algal cells. These pores are also notably consistent in size, morphology and distribution (Fig. 4B–C). This observation opens the possibility that heterogeneity in pore character and distribution were possibly dictated by differences in OM type. Description of OM type using SEM imaging has not been widely applied (e.g., Keleman et al., 2010) due to some important gaps in our understanding of OM petrography. For example, diagenetically altered and compaction-deformed organic particles of both marine and nonmarine origin may appear petrographically similar (Kennedy et al., 2002; Taylor et al., 1998). Also, there is currently no standard terminology for distinguishing structured and amorphous OM using petrographic observations (e.g., Taylor et al., 1998; Teerman et al., 1995). Chemical criteria (e.g., Tissot and Welte, 1984) remain a more generally accepted standard for defining OM type and is usually based on the hydrogen content that is bonded to organic molecules during active petroleum forming processes (Tissot and Welte, 1984). In this study, OM type is defined primarily based on chemical criteria, although petrographic features observed at high spatial resolution-SEM imaging provided further insights (e.g., Keleman et al., 2010). Based on this approach, the majority of OM concentrated in large domains/discrete intervals and stringers and

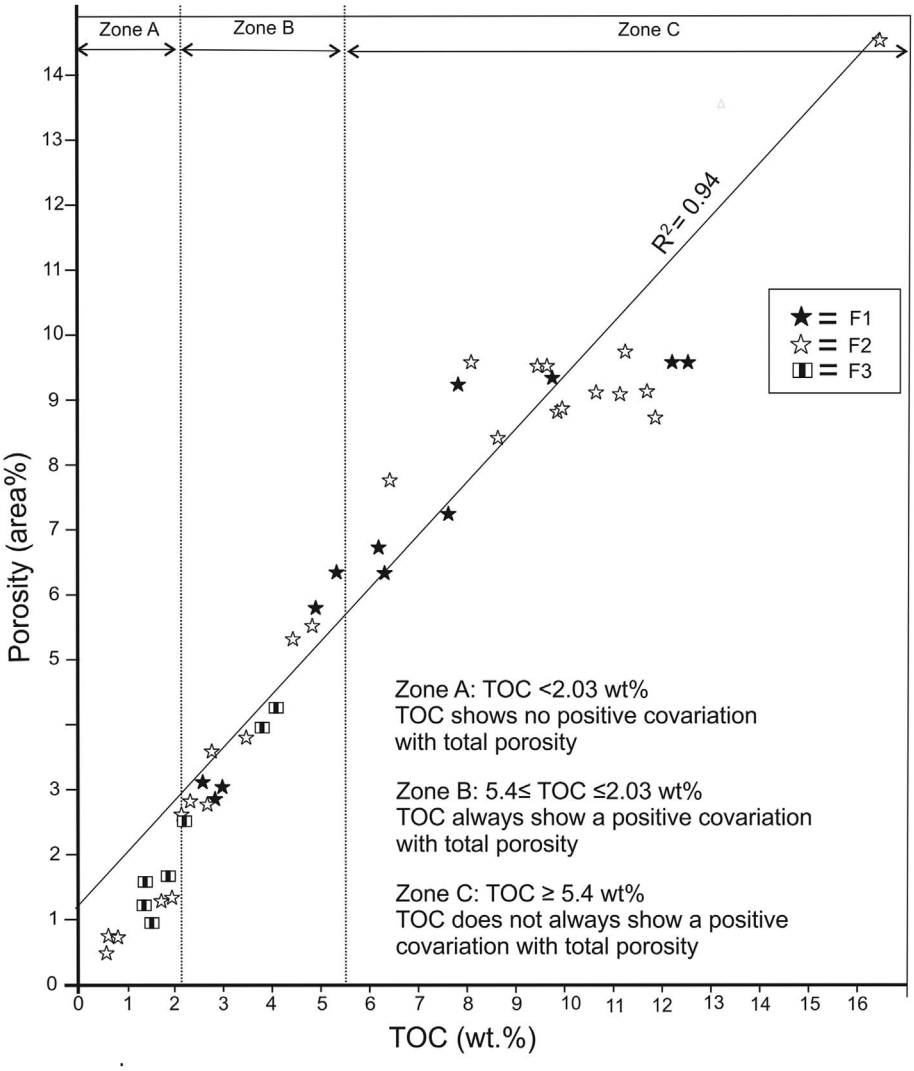

Fig. 9. Total organic carbon (TOC, wt.%) versus total porosity (area%, measured by image analysis method as described in the method section). Values of TOC between 2.03 and 5.4 wt% show stronger positive covariation with total porosity, whereas values of TOC > 5.4 wt%, covariation with total porosity becomes reduced.

some of the amorphous OM are of Type II while the small organic domains and few amorphous organic particles are of Type III (Table 2).

It is also possible to associate the observed heterogeneity in pore morphology and distribution with changes in the depositional environment (e.g., Milliken et al., 2013). Some of the sample intervals are representatives of classic low-oxygen environments where OM enrichment has been attributed to anoxic preservation (Visser, 1992; Cole and McLachlan, 1991; Scheffler et al., 2006). In anaerobic water, OM oxidation by heterotrophic microorganisms (mainly bacteria) uses nitrates and sulfates as well as fermentation (Schieber, 2011). Anaerobic oxidation results in more lipid-rich and reduced (i.e., hydrogen-rich) OM (Type II) where the preserved OM may also comprise the bacterial biomass itself. OM formed under this depositional environment yields more expellable hydrocarbons which, in turn, results in more pores and may likely explain the heterogeneity in pore character documented here.

In addition, SEM imaging of samples subjected to 68-h solvent extraction reveals marked differences in the two class of OM particles. Whereas a relative increase in pore abundance was recorded in disseminated amorphous OM, no increase was observed in the discrete, laterally continuous OM laminae. The lack of OM mobilization by dichloromethane in the latter interval may be attributed to a more complete expulsion of generated OM (bitumen) as evidenced by greater pore abundance relative to the amorphous OM. However, since a portion of the bitumen generated is usually retained (unexpelled) within the kerogen structure (e.g., Vandenbroucke and Largeau, 2007), it is likely that this difference in OM mobilization by dichloromethane is related to the inherent heterogeneity in the chemistry of the two classes of OM. The interval that shows no reaction with dichloromethane is likely infilled by an organic phase that is not willingly solvent-extractable (i.e., pyrobitumen; e.g., Vandenbroucke and Largeau, 2007; Milliken et al., 2013; Löhr et al., 2015) and different from the AOM disseminated through the shale matrix.

4.3. Thermal maturity and its impact on pore type evolution

Difference in levels of thermal maturation is another critical factor that affects porosity development in shale reservoirs (e.g., Curtis et al., 2012; Bernard et al., 2013). A plot of porosity per unit TOC (Fig. 10) across the localities studied indicates a notable reduction in porosity in samples that have experienced more advanced thermal maturation. From Fig. 10, samples with thermal maturity above 2.88 %Ro show at least 25% reduction in porosity relative to the less mature samples (% Ro < 2.88). Subject to the field of view of the sections that were investigated and within the limitations of image resolution and processing, this observation indicates that the general increase in porosity with increasing thermal maturity as documented in several shale reservoirs (e.g., Ross and Bustin, 2007; Curtis et al., 2012; Loucks et al., 2012; Bernard et al., 2013; Milliken et al., 2013) may be subject to a specific range of thermal maturity after which further increase in

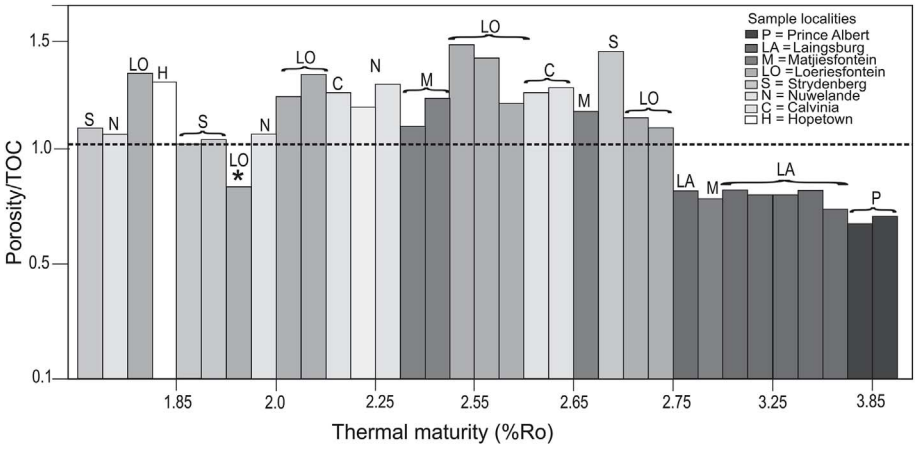

Fig. 10. Porosity per unit TOC versus thermal maturity. At thermal maturity values greater than 2.88 %Ro, porosity per unit TOC decreased by over 25%. A horizontal dotted line drawn at 1.04 represented the average value of the porosity per unit TOC to emphasize the drastic reduction in porosity in samples with thermal maturity greater than 2.88 %Ro, with the exception of one outlier (arrowed). The outlier represents the notable reduction in porosity in higher TOC samples. See text for discussion.

thermal maturity may result in dramatic reduction in the already created porosity.

4.3.1. Trends in development of organo-genetic pore types with increasing thermal maturation

The development of the pore systems (pore sizes, pore shapes, pore orientations) observed in the shale investigated, comprising both organic and nonorganic pores, appeared to represent an integral part of the depositional and diagenetic history of the shale. Studies of modern sediments suggest that freshly deposited muds are rich in water contents, up to 70–90% (e.g., Müller, 1967; Schieber, 2013). Burial compaction results in expulsion of this excess pore water and concomitant collapse of the flocculated fabrics and pore spaces. With continued burial, the preservation potential of these primary features is limited, unless where compaction is minimized by rigid grains (e.g., Schieber, 2013) or by early diagenetic precipitation of cement (e.g., Schieber, 1996). The abundance of partially compacted colonial algal cells and Tasmanites cysts (Figs. 5 and 7) preserved in pristine condition and partially infilled and intimately associated with early diagenetic cement (mostly silica) suggests that early diagenetic mobilization of silica offered protection during compaction. A likely source of the early diagenetic cement and authigenic silica, which started as fibrous chalcedony and subsequently recrystallized into quartz of various crystal sizes and shapes, is the alteration of air-fall felsic volcanic materials produced in the late Paleozoic magmatic arc of Gondwana (see Chukwuma, 2017 for further discussion on this topic). Subject to local conditions, bacterial-mediated precipitation of framboidal pyrite, carbonate and quartz grains can be triggered in the sediments during very early diagenesis by anaerobic microbial sulfate reduction (e.g., Berner, 1984). In shales with high organic contents (TOC > 5 wt.%), framework (primary) pores present in immature samples (< 0.4 %Ro) are completely filled with OM (kerogen) during the onset of oil generation as the rock is compacted, whereas shales with low (TOC < 5 wt.%), primary pores might be incompletely filled (Schieber, 2013). This explains the presence of pores in immature samples (< 0.4 %Ro), the absence of pores in certain oil-mature samples (0.5–1.1 %Ro) and the subsequent re-emergence of pore in oil- and gas-mature samples (> 0.9 %Ro) as documented in several studies (e.g., Milliken et al., 2014; Löhr et al., 2015). Also, as OM is buried, the progressive increase in temperature and pressure resulting from increasing overburden and geothermal gradient results in an increase in specific volume of the pore-fluid (Tissot and Welte, 1984; Littke et al., 1988; Jarvie et al., 2007). The increase in the volume of the pore-fluid is accompanied by an increase in pore-fluid pressure (e.g., Ungerer et al., 1983; Littke et al., 1988). Where pore-fluid pressures exceed the vertical load pressure, horizontal fractures develop (e.g., Littke et al., 1988). It is, therefore, conceivable that the horizontal microfractures and microchannels in the WHF samples developed in direct response to over-pressuring caused by hydrocarbon generation. The alignment of the majority of the fractures along bedding-planes, which are the most likely to yield to pressure, supports our opinion that their origin is related to over-pressuring. The reduction in the population of these fractures and channels in the organic-lean upper subunits of the WHF, where OM likely did not cover all available framework pores, is further evidence that these fractures are related to organic matter maturation. From this scenario, these pores were likely the first set of secondary porosity to be generated and their formation precedes significant hydrocarbon generation and thus they acted as conduits for expulsion of generated hydrocarbon, as inferred from their bitumen infills (Fig. 4F). Although most workers agree that in the post-Whitehill history of the basin, several kilometers of the Karoo Supergroup was eroded due to at least two uplift events (Rowsell and De Swart, 1976; Hanson et al., 2009; Tankard et al., 2012), these features largely rule out the possibility of associating these fractures with unloading since these uplifts postdate hydrocarbon generation in the WHF (Cole et al., 2011). The abundance of bubble and foam pores (e.g., Fig. 5) with spherical to oval cross-section suggests that their formation was related to fluid phase, presumably, conversion of OM to bitumen (Tissot and Welte, 1984; Loucks et al., 2009; Passey et al., 2010). The close spatial association between bubble and foam pores suggests a common origin (e.g., Schieber, 2013).

4.3.2. Trends in development of nonorganic pore types with increasing thermal maturation

The studied shales contain at least 10 and 3 area% of clays and carbonates, respectively (Table 1). Given this volume of clay, the phyllosilicate pores observed in the samples are typical of shale successions that have been buried sufficiently to initiate the transformation of clay minerals (e.g., smectite-to-illite) as documented by Rowsell and De Swart (1976). The smectite-to-illite transformation is usually accompanied by volume change and development of pores (e.g., Osborne and Swarbrick, 1997). The change in shale architecture (fabric and texture transformation) during the smectite-to-illite conversion thus is the likely source of the phyllosilicate pores observed (Fig. 8). The smectite-to-illite conversion overlaps with, or closely precedes the onset of kerogen (OM) transformation to bitumen (e.g., Schieber, 2013). This explains why most of the phyllosilicate pores were infilled with kerogen residue, particularly in samples with higher TOC (> 2 wt.%), whereas the majority of the phyllosilicate pores in TOC-lean samples remained open even after deep burial.

Research on pore water evolution during sediment burial (e.g., Hayes, 1991; Surdam et al., 1991; Spötl et al., 1999) suggests that smectite-to-illite transformation is closely followed by, and sometimes overlaps with, decarboxylation of kerogen, which results in accumulation of carboxylic and phenolic acids and concomitant destruction of carbonate and other framework grains. Where organic matter and its sulfur content is high, a reasonable amount of organic acids is usually

generated (Schieber, 2013), and can result in widespread corrosion and dissolution of framework grains, particularly carbonate grains and carbonate-rich clays. The dissolution pores observed in the samples (Fig. 6C–F) are similar in every aspect to those described by these authors. Therefore, it seems reasonable to conjecture that they were generated in a similar scenario. The occurrence of more complex dissolution pores (with features attributable to both dissolution and reprecipitation) in samples which experienced more advanced maturation, particularly in Prince Albert and Laingsburg localities is viewed as an evidence that their development is related to late diagenesis and advanced thermal maturation. This view is supported by the absence of diagenetic clays and calcite in these dissolution cavities, indicating that smectite-to-illite conversion must have been concluded by the time organic acid production peaked.

The dramatic reduction in porosity observed in the overmature samples (Ro > 2.88%) is inferred to be related to the large-scale infilling of the previously generated pores and fractures by fibrous crystals and residual fluid inclusions (Fig. 6C–F). The occurrence of these fibrous cements/crystals (mostly calcite and to a lesser extent silicates and phosphates) on the borders of the fractures and residual fluid inclusions trapped in the central portion indicate that the cement precipitated out of organic-rich fluid inclusions (e.g., Littke et al., 1988; Bernard et al., 2013). Similar hydrocarbon-bearing fluid inclusions have been reported in calcite-filled fractures at temperatures in excess of 180 °C (e.g., Bernard et al., 2012). These features differentiate the late diagenetic precipitates from their early diagenetic counterparts, which formed largely by the action of anaerobic microbial sulfate reduction (e.g., Berner, 1984; Schieber, 1996). The precipitation of these authigenic components and their subsequent filling of the pores created during hydrocarbon generation resulted in loss of porosity in the overmature samples and the formation of complex networks of veins. These veins, which are preferentially oriented along bedding-planes were once fractures and channels that served as conduits for expulsion of hydrocarbons. Similar calcite- and quartz-veining and fibrous cement have been documented in the WHF by previous authors in the area between Laingsburg and Prince Albert (e.g., Egle et al., 1998; Craddock et al., 2008). Geel et al. (2015) documented an extensive bedding-plane-aligned quartz-calcite veining in the WHF in the Jansenville-Prince Albert areas with geothermometry data that showed trapping temperature between 230 and 260 °C at 2–3 kb. The shale matrix porosity described here represents a fundamental parameter for gas transfer from the rock matrix to induced (artificial) fractures during gas shale stimulation programs. It can strongly impact the potential for commercial gas production and is therefore of considerable economic importance.

5. Conclusions

Two-dimensional (2-D) FE-SEM images of ultrathin sections (2 × 3 cm, 10–20 μm thick) from outcrop core samples taken from three subunits of the WHF provided both visual qualitative and semiquantitative analyses of pore systems in the potential gas shale of the WHF. Two families of pores were identified: organic and nonorganic pores. Organic pores appeared to be associated with exsolution of hydrocarbons during thermal cracking of OM and are therefore more sensitive to mechanical (compaction) diagenesis. Nonorganic pores were sensitive to chemical diagenesis (dissolution, reprecipitation, authigenesis). The development of both pore types appeared to be an integral part of the depositional and diagenetic history of the WHF. The main findings of this study are as follows:

1. Samples with < 2.03 wt.% TOC contain more nonorganic porosity than samples with > 2.03 wt.% TOC. The latter is almost entirely dominated by organic porosity. This may imply that in samples with high OM content (> 2.03 wt % TOC), primary pores were initially completely filled by nonporous OM (amorphous kerogen) that were converted to porous bitumen with organic maturation; whereas samples with lower OM content (< 2.03 wt % TOC) preserved many of the primary pores.
2. A strong positive covariation of TOC and total porosity exists in all sample localities and for all values of TOC, but particularly at TOC values between 2.03 and 5.4 wt.%. At lower or higher TOC values, the positive covariation of TOC and porosity becomes less systematic.
3. In samples with vitrinite reflectance values greater than 2.88, porosity per unit TOC decreased by over 25% relative to samples with lower thermal maturities. This indicates that the general increase in porosity with thermal maturation could be subject to a certain threshold after which residual fluid inclusion and its associated mineral precipitates may infill earlier created pores, thereby drastically reducing porosity.
4. The pore types described in this study appear to be linked to depositional and diagenetic processes common to shale units and are similar to those documented in other potential gas shale reservoirs. However, the development of bubble and foam pores, particularly those within the organo-mineral shale matrix, is unique to the WHF and was likely controlled by both OM type and diagenetic processes. The development of microfractures and microchannels, which occur mostly in the organic-rich intervals (TOC > 5 wt.%), is associated with increased pore-fluid pressure during the onset of catagenesis. Similarly, the formation of nonorganic pores such as those between clay mineral grains is associated with burial diagenesis.

Acknowledgements

The financial support of the Faculty of Science (Doctoral Fellowship) at the University of Cape Town (UCT) and the UCT Postgraduate Funding Office (travel grant) to KCh and the UCT University Research Council to EMB towards this research is hereby acknowledged. Laboratory assistance offered by Prof Chris Harris (UCT Geology Department), Prof Suryendu Dutta (Indian Institute of Technology), Suzanne Ankersjerne (SIPERG Stable Isotope Lab at Iowa State University), and staff at the Electron Microbeam Unit at Stellenbosch University, as well as insightful discussions with Prof Ayodele Asiwaju-Bello (Geology Department at Federal University of Technology Akure) are also recognized. The careful reviews provided by three anonymous reviewers as well as academic editor substantially improved the final manuscript. Opinions expressed and conclusions arrived at are those of the authors and are not necessarily to be attributed to the funders.

References

Bahadur, J., Radlinski, A.P., Melnichenko, Y.B., Mastalerz, M., Schimmelmann, A., 2015. Small-angle and ultrasmall-angle neutron scattering (SANS/USANS) study of New Albany Shale: a treatise on microporosity. Energy Fuels 29, 567–576.

Bernard, S., Horsfield, B., Schulz, H.M., Wirth, R., Schreiber, A., Sherwood, N., 2012. Geochemical evolution of organic-rich shales with increasing maturity: a STXM and TEM study of the Posidonia Shale (Lower Toarcian, northern Germany). Mar. Petrol. Geol. 31, 70–89.

Bernard, S., Wirth, R., Schreiber, A., Schulz, H.-M., Horsfield, B., 2013. FIB-SEM and TEM investigation of organic-rich shale maturation series from the Lower Toarcian Posidonia Shale, Germany: nanoscale pore system and fluid-rock interactions. In: In: Camp, W., Diaz, E., Wawak, B. (Eds.), Electron Microscopy of Shale Hydrocarbon Reservoirs, vol. 102. AAPG Memoir, pp. 53–66.

Berner, 1984. Sedimentary pyrite formation: an update. Geochim. Cosmochim. Acta 48, 143–149.

Bhattacharya, S., Dutta, S., 2015. Neoproterozoic-Early Cambrian biota and ancient niche: a synthesis from molecular markers and palynomorphs from Bikanez-Nagaur Basin, western India. Precambrian Res. 266, 36–374.

Boyer, C., Clark, B., Lewis, R., Miller, C.K., 2011. Gas shale: a global resource: oil field review. Autumn 23 (3), 26–39.

Camp, W., Diaz, E., Wawak, B., 2013. Introduction. In: In: Camp, W., Diaz, E., Wawak, B. (Eds.), Electron Microscopy of Shale Hydrocarbon Reservoirs, vol. 102. AAPG Memoir, pp. ix–xi.

Catuneanu, O., Wopfner, H., Eriksson, P.G., Cairncross, B., Rubidge, B.S., Smith, R.M.H., Hancox, P.J., 2005. The Karoo basins of south-central Africa. J. Afr. Earth Sci. 43,

211–253.
Chalmers, G.R., Bustin, M.R., Power, I.M., 2012. Characterization of gas shale pore systems by porosimetry, surface area, and field emission electron microscopy/transmission electron microscopy image analyses: examples from Barnett, Woodford, Haynesville, Marcellus, and Doig units. AAPG Bull. 96 (6), 1099–1119.
Chukwuma, K., 2017. Spatial and Temporal Variations in the Geometry and Composition of the Permian Whitehill Formation, South Africa. PhD thesis. University of Cape Town, pp. 215. http://hdl.handle.net/11427/25057.
Chukwuma, K., Bordy, E.M., 2016. Spatiotemporal sedimentary facies variations in the Permian Whitehill Formation, main Karoo Basin. In: Linol, B., de Wit, M. (Eds.), Origin and Evolution of the Cape Mountains and Karoo Basin: Geo-biohistory in a Terrain with Shale Gas Resources and Need for Conservation, Part of the Series Regional Geology Reviews 8643. Springer Verlag, pp. 101–110. http://dx.doi.org/10.1007/978-3-319-40859-0_10.
Cole, D.I., Basson, W.A., 1991. In: In: Johnson, M.R. (Ed.), Whitehill Formation in Catalogue of South African Lithostratigraphic Units, vol. 3. pp. 3.51–3.52.
Cole, D.I., McLachlan, I.R., 1991. Oil potential of the Permian Whitehill Shale Formation in the Main Karoo Basin, South Africa. In: Ulbrich, H., Rocha Campos, A.C. (Eds.), Proceedings and Papers of the Seventh Gondwana Symposium. Instituto de Geosciences, Universidade de Sao Paulo, Sao Paulo, pp. 379–390.
Cole, D.I., Robey, K., Chevallier, L., Viljoen, J., 2011. The Geology of Shales with as Gas Potential in the Main Karoo Basin of South Africa and Impact of Hydraulic Fracturing on Groundwater.
Craddock, J.P., Alex, W., McKiernan, A.W., de Wit, M.J., 2008. Calcite twin analysis in syntectonic calcite, Cape Fold Belt, South Africa: implications for fold and cleavage formation within a shallow thrust front. J. Struct. Geol. 29, 1100–1113.
Cui, Y., Kita, H., Okamoto, K., 2004. Preparation and gas separation performance of zeolite T membrane. J. Mater. Chem. 14, 924–932.
Curtis, M.E., Cardott, B.J., Sondergeld, C.H., Rai, C.S., 2012. Development of organic porosity in the Woodford Shale with increasing thermal maturity. Int. J. Coal Geol. 103, 26–31.
Demaison, G., Huizinga, B.J., 1991. Genetic classification of petroleum systems. AAPG Bull. 75, 1626–1643.
Dewhurst, D.N., Aplin, A.C., Sarda, J.P., Yang, Y.L., 1998. Compaction-driven evolution of porosity and permeability in natural mudstones: an experimental study. J. Geophys. Resour. Solid Earth 103 (B1), 651–661. https://doi.org/10.1029/97JB02540.
Egle, S., de Wit, M.J., Hoernes, S., 1998. Gondwana fluids and subsurface palaeohydrology of the Cape Fold Belt and the Karoo Basin, South Africa. J. Afr. Earth Sci. 27, 63–64.
Espitalié, J., Deroo, G., Marquis, F., 1985. Rock-Eval pyrolysis and its applications: Institut Français du Pétrole. Preprint no. 27299. .
Faure, K., Cole, D., 1999. Geochemical evidence for lacustrine microbial blooms in the vast Permian Main Karoo, Parana, Falkland Islands and Haub basins of southwestern Gondwana. Palaeogeogr. Palaeoclimatol. Palaeoecol. 152, 189–213.
Fishman, N.S., Hackley, P.C., Lowers, H.A., Hill, R.J., Egenhoff, S.O., Eberl, D.D., Blum, A.E., 2012. The nature of porosity in organic-rich mudstones of the Upper Jurassic Kimmeridge Clay Formation, North Sea, offshore United Kingdom. Int. J. Coal Geol. 103, 32–50.
Geel, C., de Wit, M., Booth, P., Schulz, H.-M., Horsfield, B., 2015. Palaeo-environment, diagenesis and characteristics of Permian black shales in the lower Karoo Supergroup flanking the Cape Fold Belt near Jansenville, Eastern Cape, South Africa: implications for the shale gas potential of the Karoo Basin. S. Afr. J. Geol. 118, 248–274.
Hanson, E.K., Moore, J.M., Bordy, E.M., Marsh, J.S., Howarth, G., Robey, J.V.A., 2009. Cretaceous erosion in central South Africa: evidence from upper-crustal xenoliths in kimberlite diatremes. S. Afr. J. Geol. 112, 125–140.
Hayes, J.B., 1991. Porosity evolution of sandstones related to vitrinite reflectance. Org. Geochem. 17, 117–129.
Injuk, J., Van Grieken, R., 1993. Sample preparation for XRF. In: Van Grieken, R.E., Markowicz, A.A. (Eds.), Handbook of X-Ray Spectrometry: Methods and Techniques. Marcel Dekker, Inc, New York, NY, pp. 657–692.
IAEA (International Atomic Energy Agency), 1997. Sampling, Storage, Sample Preparation Procedures for X-ray Fluorescence Analysis of Environmental Materials. IAEA-TECDOC- 950, Vienna.
IUPAC (International Union of Pure and Applied Chemistry), 1994. Physical chemistry division commission on colloid and surface chemistry, subcommittee on characterization of porous solids: recommendations for the characterization of porous solids (technical report). Pure Appl. Chem. 66 (8), 1739–1758.
Jarvie, D.M., Claxton, B.L., Henk, F., Breyer, J.T., 2001. Oil and shale gas from the Barnett Shale, Ft. Worth Basin, Texas. Talk presented at the AAPG National Convention, June 3-6, 2001. AAPG Bull. A100.
Jarvie, D.M., Hill, R.J., Ruble, T.E., Pollastro, R.M., 2007. Unconventional shale-gas systems: the Mississippian Barnett Shale of north-central Texas as one model for thermogenic shale gas assessment. AAPG Bull. 91 (4), 475–499.
Kaufhold, S., Grathoff, G.H., Halisch, M., Plötze, M., Kus, J., Ufer, K., Dohrmann, R., Ladage, S., Ostertag-Henning, C., 2016. Comparison of methods for the determination of the pore system of a potential German gas shale. In: The Clay Minerals Society Workshop Lecture Series, vol. 21. pp. 163–190. http://dx.doi.org/10.1346/CMS.
Keleman, S.R., Walters, C.C., Kwiatek, P.J., Freund, H., Afeworki, M., Sansome, M., Lamberti, W.A., Pottorf, R.J., Mchel, H.G., Peters, P.E., Bolin, T., 2010. Characterization of solid bitumens originating from thermal chemical alteration and thermochemical sulfate reduction. Geochim. Cosmochim. Acta 74, 5305–5332. http://dx.doi.org/10.1016/j.gca .2010.06.013.
Keller, L.M., Holzer, L., Wepf, R., Gasser, P., 2011. 3D geometry and topology of pore pathways in Opalinus clay: implications for mass transport. Appl. Clay Sci. 52, 85–95.
Kennedy, M.J., Pevear, D.R., Hill, R.J., 2002. Mineral surface control of organic carbon in black shale. Science 295, 657–660. http://dx.doi.org/10.1126/science.1066611.
Klaver, J., Desbois, G., Urai, J.L., Littke, R., 2012. BIB-SEM study of the pore space morphology in early mature Posidonia Shale from the Hils area, Germany. Int. J. Coal Geol. 103, 12–25.
Klemme, H.D., Ulmisheck, G.F., 1991. Effective petroleum source rocks of the world: stratigraphic distribution and controlling factors. AAPG Bull. 75, 1809–1851.
Könitzer, S.F., Leng, M.J., Davies, S.J., Stephenson, M.H., 2012. An assessment of geochemical preparation methods prior to organic carbon concentration and carbon isotope ratio analyses of fine-grained sedimentary rocks. Geochem. Geophys. Geosyst. 13, Q0AI02. http://dx.doi.org/10.1029/2012GC004094.
Lazar, O.R., Bohacs, K.M., Macquaker, J.H.S., Schieber, J., Demko, T.M., 2015. Capturing key attributes of fine-grained sedimentary rocks in outcrops, cores, and thin sections: nomenclature and description guidelines. J. Sediment. Res. 85, 230–246.
Littke, R., Baker, D.R., Leythaeuser, D., 1988. Microscopic and sedimentologic evidence for the generation and migration of hydrocarbons in Toarcian source rocks of different maturities. Org. Geochem. 13, 549–559.
Löhr, S.C., Baruch, E.T., Hall, P.A., Kennedy, M.J., 2015. Is organic pore development in gas shales influenced by primary porosity and structure of thermally immature organic matter? Org. Geochem. 87, 119–132.
Loucks, R.G., Reed, R.M., Ruppel, S.C., Jarvie, D.M., 2009. Morphology, genesis, and distribution of nanometer scale pores in mudstones of the Mississippian Barnett Shale. J. Sediment. Res. 79, 848–861. http://dx.doi.org/10.2110/jsr.2009.092.
Loucks, R.G., Reed, R.M., Ruppel, S.C., Hammes, U., 2012. Spectrum of pore types and networks in mudrocks and a descriptive classification for matrix-related mudrock pores. AAPG Bull. 96, 1071–1098.
Magoon, L.B., Dow, W.G. (Eds.), 1994. The Petroleum System-from Source to Trap, vol. 60. AAPG Memoir, pp. 1–24.
Mastalerz, M., Schimmelmann, A., Drobniak, A., Chen, Y., 2013. Porosity of Devonian and Mississippian New Albany Shale across a maturation gradient: insights from organic petrology, gas adsorption, and mercury intrusion. AAPG Bull. 97, 1621–1643.
Meyers, P.A., 1997. Organic geochemical proxies of paleoceanographic, paleolimnologic, and paleoclimatic processes. Org. Geochem. 276 (5/6), 213–250.
Milliken, K.L., Rudnicki, M., Awwiller, D.N., Zhang, T., 2013. Organic matter-hosted pore system, Marcellus Formation (Devonian), Pennsylvania. AAPG Bull. 97, 177–200.
Milliken, K.L., Ko, L.T., Pommer, M., Marsaglia, K.M., 2014. SEM Petrography of Eastern Mediterranean sapropels: analogue data for assessing organic matter in oil and gas shales. J. Sediment. Res. 84, 961–974.
Müller, G., 1967. Diagenesis in argillaceous sediments. In: In: Larsen, G., Chilingar, G.U. (Eds.), Diagenesis in Sediments, Developments in Sedimentology, vol. 8. Elsevier, Amsterdam, pp. 127–178.
Oelofsen, B.W., 1981. An Anatomical and Systematic Study of the Family Mesosauridae (Reptilia, Proganosauria) with Special Reference to its Associated Fauna and Palaeoecological Environment in the Whitehill Sea. Unpublished Ph.D. thesis. University of Stellenbosch, pp. 163. http://hdl.handle.net/10019.1/69984.
Osborne, M.J., Swarbrick, R.E., 1997. Mechanisms for generating overpressure in sedimentary basins: a Reevaluation. AAPG Bull. 81, 1023–1041.
Passey, Q.R., Bohacs, K.M., Esch, W.L., Kimentidis, R., Sinha, S., 2010. From oil-prone source rock to gas-producing shale reservoir: geologic and petrophysical characterization in unconventional shale-gas reservoirs. In: Chinese Petroleum Society/Society of Petroleum Engineers International Oil & Gas Conference and Exhibition, Beijing, China, June 8-10, 2010, pp. 29 SPE Paper 121250, doi:102118/131350-MS.
Radke, M., WeRe, D.H., Willscli, H., 1986. Maturity parameters based on aromatic hydrocarbons: influence of the organic matter type. In: In: Leythaeuser, D., Rullktter, J. (Eds.), Advances in Organic Geochemistry 1985, vol. 10. Pergamon Press, Oxford, pp. 51–64 Organic Geochemistry.
Ross, D.J.K., Bustin, R.M., 2007. Impact of mass balance calculations on adsorption capacities in microporous shale gas reservoirs. Fuel 86, 2696–2706.
Rowsell, D.M., De Swart, A.M.J., 1976. Diagenesis in Cape and Karroo sediments, South Africa, and its bearing on their hydrocarbon potential. Trans. Geol. Soc. S. Afr. 79, 81–145.
SACS (South African Committee for Stratigraphy), 1980. Stratigraphy of South Africa, Part 1. L.E. Kent (Compiler), Handbook Geological Survey of South Africa, Pretoria, 8, 690 p.
Scheffler, K., Bühmann, D., Schwark, L., 2006. Analysis of late Palaeozoic glacial to postglacial sedimentary succession in South Africa by geochemical proxies-Response to climate evolution and sedimentary environment. Palaeogeogr. Palaeoclimatol. Palaeoecol. 240, 184–203.
Schieber, J., 1996. Early diagenetic silica deposition in algal cysts and spores: a source of sand in black shales? J. Sediment. Res. 66, 175–183.
Schieber, J., 2011. Shale Microfabrics and Pore Development -An Overview with Emphasis on the Importance of Depositional Processes. Recovery-2011 CSPG CSEG CWLS Convention. .
Schieber, J., 2013. SEM Observations on ion-milled samples of Devonian Black Shales from Indiana and New York: the petrographic context of multiple pore types. In: In: Camp, W., Diaz, E., Wawak, B. (Eds.), Electron Microscopy of Shale Hydrocarbon Reservoirs, vol. 102. AAPG Memoir, pp. 153–171.
Schieber, J., Zimmerle, W., 1998. Introduction and overview: the history and promise of shale research. In: Schieber, J., Zimmerle, W., Sethi, P. (Eds.), Shales and Mudstones, Volume I. Basin Studies, Sedimentology, and Paleontology. E. Schweizerbart'sche Verlagsbuchhandlung (Nagele u. Obermiller), Stuttgart, pp. 1–10.
Schieber, J., Krinsley, D., Riciputi, L., 2000. Diagenetic origin of quartz silt in mudstone and implication for silica cycling. Nature 406, 981–985.
Spötl, C., Longstaffe, F.J., Ramseyer, K., Rudinger, B., 1999. Authigenic albite in carbonate rocks- a tracer for deep-burial brine migration? Sedimentology 46 (4), 649–666.
Sommacal, S., Fogden, A., Young, B., Noel, W., Arena, A., Salazar, L., Gerwig, T., Cheng, Q., Kingston, A., Marchal, D., Perez Mazas, A.M., Naides, C.H., Kohler, G., Cagnolatti,

M., 2016. 3D multiscale imaging of the distribution of pores, organic matter and oil in place in Vaca Muerta shale samples. In: Unconventional Resources Technology Conference, San Antonio, TX, August 2016, pp. 2564–2579 URTEC-2460975.
Surdam, R.C., MacGowan, D.B., Dunn, T.L., 1991. Predictive models for sandstone diagenesis. Org. Geochem. 17, 243–253.
Tankard, A., Welsink, H., Aukes, P., Newton, R., Stettler, E., 2012. Geodynamic Interpretation of the Cape and the Karoo Basins, South Africa, Phanerozoic Passive Margins, Cratonic Basins and Global Tectonics Maps. Elsevier, USA and UK, pp. 869.
Tappan, H., 1980. The Paleobiology of Plant Protists. W.H. Freeman and co., San Francisco, pp. 1028.
Taylor, G.H., Teichmüller, M., Davis, A., Diessel, C.F.K., Littke, R., Robert, P., 1998. Organic Petrology. Gebrüder Borntraeger, Berlin.
Teerman, S.C., Cardott, B.J., Harding, R.W., Lemos De Sousa, M.J., Logan, D.R., Pinheiro, H.J., Reinhardt, M., Thompson-Rizer, C.L., Woods, R.A., 1995. Source rock/dispersed organic matter characterization: TSOP research subcommittee results. Org. Geochem. 22, 11–25. http://dx.doi.org/10.1016/0146-6380(95)90004-7.
Telnova, O.P., 2012. Morphology and ultrastructure of Devonian prasinophycean algae (Chlorophyta). Paleontol. J. 46, 543–548.
Tissot, B.P., Welte, D.H., 1984. Petroleum Formation and Occurrence. Springer Verlag, Berlin, Germany, pp. 699.
Ungerer, P., Behar, E., Discamps, D., 1983. Tentative calculation of the overall volume expansion of organic matter during hydrocarbon genesis from geochemistry data: implications for primary migration. In: Bjorøy, M. (Ed.), Advances in Organic Geochemistry, 1981. Wiley, Chichester, pp. 129–135.
US National Petroleum Council (NPC), 2007. Unconventional Gas Reservoirs- Tight Gas, Coal Seams, Shales. Working Document of NPC Global Oil and Gas Supply. Topic paper no. 29, Washington, D.C. .
US-EIA (V. Kuuskraa, S. Stevens, T. Van Leeuwen, and K. Moodhe), 2011. World Shale Gas Resources: an Initial Assessment of 14 Regions outside of the United States. US DOE, EIA Open file, Assessed March 2014.
Vandenbroucke, M., Largeau, C., 2007. Kerogen origin, evolution and structure. Org. Geochem. 38, 719–833.
Visser, J.N.J., 1992. Deposition of the Early to Late Permian Whitehill Formation during a sea- level highstand in a juvenile foreland basin. S. Afr. J. Geol. 95, 181–193.
Walls, J.D., Sinclair, S.W., 2011. Eagle Ford shale reservoir properties from digital rock physics. First Break 29, 97–101.
Wright, M.C., Court, R.W., Kafantris, F.-C.A., Spathopoulos, F., Sephton, M.A., 2015. A new rapid method for shale oil and shale gas assessment. Fuel 153, 231–239.